

 Open access • Posted Content • DOI:10.1101/2021.02.24.432759

Implications of central carbon metabolism in SARS-CoV-2 replication and disease severity — [Source link](#)

Shuba Krishnan, Hampus Nordqvist, Anoop T. Ambikan, Soham Gupta ...+19 more authors

Institutions: Karolinska Institutet, Science for Life Laboratory, Indian Institute of Science, Karolinska University Hospital ...+1 more institutions

Published on: 24 Feb 2021 - bioRxiv (Cold Spring Harbor Laboratory)

Topics: Viral replication, Glutaminolysis, Metabolic pathway and Virus

Related papers:

- [Metabolic Perturbation Associated With COVID-19 Disease Severity and SARS-CoV-2 Replication.](#)
- [Mitochondrial metabolic manipulation by SARS-CoV-2 in peripheral blood mononuclear cells of patients with COVID-19.](#)
- [Host metabolic reprogramming in response to SARS-CoV-2 infection: A systems biology approach.](#)
- [Host metabolic reprogramming in response to SARS-Cov-2 infection](#)
- [An untargeted metabolomic approach to identify antiviral defense mechanisms in memory leukocytes secreting in vitro IgG anti-SARS-Cov-2](#)

Share this paper:    

View more about this paper here: <https://typeset.io/papers/implications-of-central-carbon-metabolism-in-sars-cov-2-t89xlw1xab>

1 **Implications of central carbon metabolism in SARS-CoV-2 replication and** 2 **disease severity**

3
4 **Authors:** Shuba Krishnan¹, Hampus Nordqvist², Anoop T. Ambikan¹, Soham Gupta¹, Maike
5 Sperk¹, Sara Svensson-Akusjärvi¹, Flora Mikaeloff¹, Rui Benfeitas³, Elisa Saccon¹, Sivasankaran
6 Munusamy Ponnann⁴, Jimmy Esneider Rodriguez⁵, Negin Nikouyan¹, Amani Odeh⁶, Gustaf
7 Ahlén¹, Muhammad Asghar⁶, Matti Sällberg¹, Jan Vesterbacka⁷, Piotr Nowak^{7,8}, Ákos Végvári⁵,
8 Anders Sönnérborg^{1,6}, Carl Johan Treutiger^{2,7}, Ujjwal Neogi^{1*}

9 10 **Affiliations:**

11 ¹Division of Clinical Microbiology, Department of Laboratory Medicine, Karolinska Institute,
12 ANA Futura, Campus Flemingsberg, S-14152 Stockholm, Sweden.

13 ²Södersjukhuset (The South General Hospital), Stockholm, Sweden.

14 ³National Bioinformatics Infrastructure Sweden (NBIS), Science for Life Laboratory, Department
15 of Biochemistry and Biophysics, Stockholm University, S-10691 Stockholm, Sweden.

16 ⁴Centre for Infectious Disease Research, Indian Institute of Science (IISc), CV Raman Avenue,
17 Bangalore, India.

18 ⁵Division of Chemistry I, Department of Medical Biochemistry and Biophysics, Karolinska
19 Institutet, SE-171 65 Stockholm, Sweden.

20 ⁶Division of Infectious Diseases, Department of Medicine Solna, Karolinska Institutet,
21 Stockholm, Sweden

22 ⁷Department of Medicine Huddinge, Division of Infectious Diseases, Karolinska Institute, I73,
23 Karolinska University Hospital, Huddinge, 141 86 Stockholm, Sweden.

24 ⁸The Laboratory for Molecular Infection Medicine Sweden MIMS, Umeå University, Sweden.

25

26 *To whom correspondence should be addressed: Ujjwal Neogi (ujjwal.neogi@ki.se)

27

28

29 **Short Title:** COVID-19 and central carbon metabolism

30

31 **Abstract**

32 Viruses hijack host metabolic pathways for their replicative advantage. Several observational
33 trans-omics analyses associated carbon and amino acid metabolism in coronavirus disease 2019
34 (COVID-19) severity in patients but lacked mechanistic insights. In this study, using patient-
35 derived multi-omics data and *in vitro* infection assays, we aimed to understand i) role of key
36 metabolic pathways in severe acute respiratory syndrome coronavirus-2 (SARS-CoV-2)
37 reproduction and ii) its association with disease severity. Our data suggests that monocytes are
38 key to the altered immune response during COVID-19. COVID-19 infection was associated with
39 increased plasma glutamate levels, while glucose and mannose levels were determinants of the
40 disease severity. Monocytes showed altered expression pattern of carbohydrate and amino acid
41 transporters, GLUT1 and xCT respectively in severe COVID-19. Furthermore, lung epithelial
42 cells (Calu-3) showed a strong acute metabolic adaptation following infection *in vitro* by
43 modulating central carbon metabolism. We found that glycolysis and glutaminolysis are essential
44 for virus replication and blocking these metabolic pathways caused significant reduction in virus
45 production. Taken together, our study highlights that the virus utilizes and re-wires pathways
46 governing central carbon metabolism leading to metabolic toxicity. Thus, the host metabolic
47 perturbation could be an attractive strategy to limit the viral replication and disease severity.

48 **Introduction**

49 The global pandemic of coronavirus disease 2019 (COVID-19) caused by the severe acute
50 respiratory syndrome coronavirus-2 (SARS-CoV-2) created a severe public health crisis
51 worldwide. Although most patients presented with mild to moderate or no symptoms, patients
52 having pre-existing metabolic disorders like diabetes, cardiovascular diseases, and obesity are at
53 risk for severe and critical cases of infection. Some recent observational studies indicate that
54 disease severity in COVID-19 patients are associated with plasma metabolic abnormalities that
55 include a shift towards amino acid and fatty acid synthesis, altered energy and lipid metabolism
56 [1-3] and metabolic profile can identify the disease severity [4]. However, metabolic regulation
57 of an individual always depends on several factors including age, gender, environmental factors,
58 dietary intake and lifestyle. Such alterations in metabolic regulation can change rapidly or adapt
59 to an altered situation and sometimes have sustained effects over an extended period. The initial
60 phase of characterization of the metabolic landscape of COVID-19 and its association with
61 disease severity has urged the need to understand how metabolic reprogramming occurs during
62 the acute SARS-CoV-2 infection with the ultimate goal towards therapeutic intervention.

63 Viruses are known to exploit the host metabolic machinery to meet their biosynthetic demands
64 for optimal replication capacity. This cellular exploration is highly connected with the initial
65 host-viral response, thereby determining the disease pathogenesis. Viral replication is dependent
66 on extracellular carbon sources such as glucose and glutamine. It induces a plethora of metabolic
67 alterations in host-cell including host central carbon metabolism, nucleotide, fatty acids and lipid
68 synthesis that modulate viral pathogenesis and host-response [5, 6]. Recent *in vitro* multi-omics
69 studies have shown that the SARS-CoV-2 dysregulates PI3K/Akt/mTOR and HIF-1 signaling in
70 infected cells. These pathways regulate glycolysis by altering glucose transporters (GLUT) across

71 cell membranes. Targeting these pathways with inhibitors such as MK2206 (Akt inhibitor) or 2-
72 deoxy-D-glucose (2-DG, glycolysis inhibitor) can lower the viral burden in the cells *in vitro* [7,
73 8]. This opens the area for host-based metabolic strategies to inhibit viruses as an additional way
74 other than direct-acting antivirals to weaken the viral replication by metabolic intervention.
75 In this study, we performed plasma proteomics targeting 92 plasma proteins related to
76 inflammation and plasma untargeted metabolomics followed by immune phenotyping of the
77 lymphocyte and monocyte cell population towards the metabolite transporters. We also
78 performed quantitative untargeted proteomics studies *in vitro* by infecting lung, liver, kidney, and
79 colon cells with the SARS-CoV-2 virus to understand the viral-induced metabolic rewiring. We
80 also modulate the key metabolic pathways identified in the patient-based metabolomics data and
81 cell-model based quantitative proteomics data to regulate the viral reproduction. Our clinical and
82 experimental studies thus provided an account of metabolic control during SARS-CoV-2
83 infection that can aid antiviral therapeutics in COVID-19 through metabolic perturbation.

84

85 **Results**

86 **Patient characteristics**

87 The study population included healthy controls (HC, n=31), SARS-CoV-2 PCR positive
88 hospitalized-mild (mild, O₂ consumption<4lit/min, n=29) and hospitalized-severe (severe, O₂
89 consumption≥4lit/min, n=12) patients. The mild and severe groups were matched by gender
90 (male: 79% vs 91%, p=0.6514), BMI [median (IQR): 29 (25-31) vs 28 (25-34); p=0.8622] and
91 age [median (IQR): 57 (44-63) vs 57 (52-69); p=0.2831]. The HC has significantly lower age
92 [median (IQR): 48 (46-55)], lower BMI [median (IQR): 24 (21-25)] (Table S1). The IgG CoV-2
93 antibody test showed 10 of the HC were CoV-2 antibody positive (HC-CoV-2 Ab+, Fig S1).

94 Among the COVID-19 patients, the classical co-morbidities were observed at 45% (13/29) in
95 mild and at 66% (8/12) in severe ($p=0.3058$). The samples were collected within median (IQR) 2
96 (2-3.5) days of hospitalization [median (IQR) mild: 2 (1-3) and severe 3 (2-4); $p=0.1170$].

97 **Plasma proteomics identified distinct clusters of HC and COVID-19 individuals**

98 We performed targeted proteomics analyses (secretome) looking at 92 plasma proteins involved
99 in inflammatory responses. As expected, several cytokines and chemokines were significantly
100 elevated in COVID-19 patients (mild and severe) compared to HCs (HC and HC-CoV-2 Ab+),
101 including IL-6 (Fig 1a). Pathway enrichment analyses of the proteins that were significantly
102 changed between HCs and COVID-19 patients revealed that the majority of altered proteins were
103 involved in cytokine-cytokine receptor interaction and chemokine signaling, followed by
104 intestinal network for IgA production, IL-17 signaling pathway, and Toll-like receptor signaling
105 pathway; to name the top five pathways (Fig 1b). Interestingly, 11 proteins were altered between
106 the mild and severe COVID-19 patients (Fig 1a and 1c): hepatocyte growth factor (HGF),
107 pleiotrophin (PTN), the chemokines CXCL12, CXCL13, and CCL23 (also known as macrophage
108 inflammatory protein 3 or MIP-3), monocyte-chemotactic protein (MCP-3, also known as
109 CCL7), interleukin 12 (IL-12), tumor necrosis factor-like weak inducer of apoptosis (TWEAK),
110 vascular endothelial growth factor A (VEGFA), angiopoietin 2 (ANGPT2), and Fas ligand
111 (FASLG) (adj $p<0.05$). The majority of these proteins were elevated in COVID-19 patients with
112 highest levels in the severe group, except for IL-12 which was increased in the mild group
113 compared to both severe group and HCs (Fig 1a and 1b). Further, FASLG followed the opposite
114 trend of being lower in COVID-19 patients compared to HC and lowest in severe COVID-19
115 patients. This data showed that although IL-12 levels were increased in COVID-19 patients

116 compared to HC, the COVID-19 severe patients had reduced IL-12 compared to the mild
117 patients.

118 **Distinct amino acid and carbohydrate profile in COVID-19 patients**

119 The plasma metabolomic profile followed a pattern similar to the plasma proteomics. However,
120 no metabolites were significantly different between HC and HC-CoV-2 Ab+ (adj $p > 0.05$).
121 Therefore we combined the two groups as HC for further analysis. The distribution of all samples
122 for metabolite enrichment showed a fair separation between samples of HC and COVID-19
123 patients (Fig 2a). Differential analysis between COVID-19 patients and healthy individuals after
124 adjusting for age, gender, and BMI identified 444 significantly regulated metabolites (adj
125 $p < 0.05$), many of which are lipids followed by amino acids (Fig 2b). Metabolite set enrichment
126 analysis of the significant metabolites (adj $p < 0.05$) identified amino acid-related pathways were
127 most predominantly affected during infection, as shown in Fig 2c. Hierarchical clustering of the
128 metabolites showed two clusters that had distinct enrichment patterns in COVID-19 infected
129 patients compared to HCs (Fig 2d). Among these, amino acids such as glycine, proline,
130 tryptophan, alanine, histidine, glutamine and arginine had lower levels in COVID-19 patients,
131 while glutamate, aspartate and phenylalanine had higher levels (Fig 2d and S2) as also observed
132 in earlier studies [1, 3, 9]. Interestingly, metabolites of the central carbon metabolism including
133 glycolysis (glucose, 3-phosphoglycerate, pyruvate, lactate) and tricarboxylic acid (TCA) cycle
134 (citrate, aconitate, α -ketoglutarate) showed distinct changes when comparing HCs and COVID-
135 19 patients and the different COVID-19 disease states (Fig S3).

136 **Severe COVID-19 patients show a distinct metabolic profile with mannose as a biomarker**

137 Next, we aimed to identify the metabolic signature in COVID-19 severe patients. Statistical
138 analysis found 88 metabolites that significantly differed in the severe group compared to mild

139 samples. Hierarchical clustering of the metabolites showed two clusters with moderately distinct
140 enrichment patterns in severe samples compared to mild samples (Fig 3a). Metabolic pathway
141 enrichment analysis of the significant metabolites by IPA showed that several amino acid-related
142 pathways, IL-12 signaling and production in macrophages and insulin signaling pathways were
143 mainly dysregulated in the severe patient samples compared to mild ones (Fig 3b). Next, we
144 sought to identify biomarkers that differentiate the severe and mild samples. Using R package
145 MUVR that is suitable for small sample size, a total of eight metabolites were identified as
146 biomarkers (Fig S4). After adjusting for age, gender and BMI, seven remained significant of
147 which four had higher abundance and three had lower abundance in COVID-19 severe patients
148 compared to the mild ones (Fig 3c and S4). Mannose was identified as one of the biomarkers of
149 disease severity, being upregulated in COVID-19 infection and also in severe patients compared
150 to mild ones. COVID-19 infection was associated with increased glutamate levels while glucose
151 and mannose were determinants of the severity of the disease (Fig 3d and 3e). This data suggests
152 alterations in the glycolysis/gluconeogenesis, glutaminolysis and mannose metabolism in
153 COVID-19 patients irrespective of severity.

154 **Increased mannose-binding lectin (MBL) in COVID-19 patients without any correlation** 155 **with mannose levels**

156 Plasma mannose can bind to several C-type lectins (*e.g.* MBL) and play an important role in viral
157 pathogenesis by recognizing glycans present in the viral envelope and subsequently activating
158 antiviral immune response and T-cells [10, 11]. Our targeted secretome data identified the C-type
159 lectin receptor signaling pathway as one of the top 28 ranked protein pathways that were
160 significantly changed between HCs and COVID-19 patients (Fig 1b). We, therefore, measured
161 plasma levels of soluble MBL using ELISA and observed an increase in COVID-19 patients

162 compared to HC. Strikingly, there was no significant difference between the mild and severe
163 COVID-19 patients, but the HC-CoV-2 Ab+ individuals showed increased MBL levels compared
164 to HC (Fig 3f). This data shows a prominent elevation of MBL during COVID-19 infection that
165 can persist over a prolonged duration of time after recovery. We did not observe any correlation
166 between MBL and mannose in COVID-19 patients [Spearman correlation: 0.1437 (95%CI: -
167 0.1806 - 0.4399)]. We, therefore, speculate that elevated MBL might not directly be the
168 consequence of the higher plasma mannose levels but regulated by SARS-CoV-2.

169 **Immune phenotyping of glucose, glutamate, and mannose transporters**

170 Metabolite transporters are known to dictate immune cell activity by controlling access to
171 nutrients, thereby maintaining cellular homeostasis [12]. Therefore, we next measured the
172 expression of glucose/mannose and glutamate transporters that were associated with
173 SARS-CoV-2 infection or disease severity, GLUT1 (SLC2A1) and xCT (SLC7A11) respectively,
174 in PBMCs of HC (n=19), HC-CoV-2 Ab+ (n=9) and COVID-19 patients: mild (n=21) and severe
175 (n=11) using flow cytometry. The relative frequency of lymphocytes significantly decreased in
176 COVID-19 patients than HCs, which was more prominent in severe patients (Fig 4a). In total
177 lymphocytic populations the CD3⁺ T-cells were significantly reduced in COVID-19 severe
178 patients compared to mild patients and HCs (Fig 4b). Although there was no difference in total
179 monocyte frequencies, we observed a mild increase in the frequency of intermediate monocytes
180 and a significant decrease in non-classical monocytes in the COVID-19 patients than HCs (Fig 4a
181 and 4b). This highlights the potential role of monocytes in COVID19 as was also recently
182 reported in single-cell transcriptomics data [4] and functional analysis on COVID-19 patient
183 monocytes [13].

184 More than 98% CD8⁺ T-cells expressed GLUT1, and the surface expression of GLUT1 was
185 significantly higher in COVID-19 severe patients than mild and HCs (Fig 4c and 4d). We also
186 found increased frequencies of intermediate and non-classical monocytes expressing GLUT1 and
187 significantly higher surface expression of GLUT1 on the intermediate monocytes of COVID-19
188 severe patients compared to HCs (Fig 4c and 4d). While all classical and intermediate monocytes
189 expressed xCT, we observed decreased frequency of non-classical monocytes expressing xCT in
190 COVID-19 patients compared to HCs (Fig 4e). The surface expression of xCT was higher in
191 classical and intermediate subpopulations of COVID-19 patients than HCs (Fig 4f), emphasizing
192 the role of metabolite transporters in monocytes in COVID-19 infection and disease severity.

193 **SARS-CoV-2 regulates central carbon metabolic pathways in a cell-type-specific manner**

194 Our previous study, together with other observational studies, indicate that SARS-CoV-2
195 infection causes dysregulation of PI3K/Akt/mTOR and HIF-1 signaling pathway [7, 14, 15], and
196 affect mitochondrial functions [13, 16]. Based on these findings, we hypothesized that the altered
197 extracellular glucose, mannose and glutamate levels are due to dysregulated carbohydrate
198 metabolism and mitochondrial function. Therefore, to identify the acute host cellular response to
199 the SARS-CoV-2 infection we infected different human cell lines including Calu-3 (lung), Caco-
200 2 (colon), 293FT (kidney) and Huh7 (liver) followed by untargeted quantitative proteomics 24
201 hours post-infection (hpi) at multiplicity of infection (moi) of 1 [17]. Differential protein
202 abundance analysis identified 6462 proteins differentially expressed in Calu-3, 177 in Caco-2,
203 four in Huh7 and none in 293FT following 24 hpi. This data indicated an acute response
204 predominantly in the lung cells that are the primary site of SARS-CoV-2 infection. The protein
205 set enrichment analysis restricted to metabolic pathways identified that most of the highly
206 abundant proteins in infected Calu-3 cells belonged to pentose phosphate pathway (PPP), fructose

207 and mannose metabolism, as well as amino acid biosynthesis (Fig 5a). Proteins detected at a
208 lower level in the infected cells mainly belonged to TCA cycle, oxidative phosphorylation and
209 N-glycan biosynthesis (Fig 5a). Parallely, in patients' metabolomic analysis we observed
210 unbalanced levels of glycolysis, fructose and mannose metabolism and TCA cycle intermediates
211 (Fig 2d and 3d). We, therefore, focused our analysis on the proteins (n=78) that are a part of
212 glycolysis/gluconeogenesis, fructose and mannose metabolism and TCA cycle (KEGG Human
213 2019) (Fig 5b). A clear change in metabolic poise was observed upon SARS-CoV-2 infection in
214 Calu-3 cells where a majority of the significantly upregulated proteins belonged to
215 glycolysis/gluconeogenesis and fructose and mannose metabolism while most of the proteins of
216 the TCA cycle were significantly downregulated (Fig 5b and S5). However this phenomenon was
217 not observed in the other three cell culture models (Fig S6). Only two out of 177 proteins
218 identified were significantly different in Caco-2 cells (ACSS1 and PFKFB4) and no differences
219 were observed in Huh7 cells out of the four identified proteins in the three pathways mentioned
220 above (Fig S6). This shows that Calu-3 cells, which are lung epithelial cells, have a distinct
221 metabolic modulation caused by SARS-CoV-2 infection. Interestingly, although all the
222 mitochondrial TCA cycle enzymes were downregulated, cytosolic enzymes such as MDH1,
223 IDH1, ACO1 and ACLY that convert TCA cycle intermediates outside the mitochondria were
224 upregulated in infected Calu-3 cells (Fig 5c). This points towards dysfunctional mitochondria
225 caused by COVID-19 infection. Alterations in mitochondrial DNA (mtDNA) copy number in
226 circulating blood cells can serve as a surrogate for mitochondrial dysfunction [18]. Indeed in our
227 patient cohort we observed a decreasing trend of the mtDNA copy numbers with the disease
228 severity (Fig 5d). In addition to changes in glucose and glutamate (Fig 3d), we also observed a
229 significant increase in metabolites such as pyruvate, lactate and α -ketoglutarate (more
230 pronounced in mild patients) and decrease in citrate and aconitate in COVID-19 patients

231 compared to HCs (Fig S6). This indicated an impact of SARS-CoV-2 infection on glycolysis and
232 glutaminolysis to meet biosynthetic and bioenergetic demands. In order to determine the
233 requirement of glycolysis and glutaminolysis for optimal replication of SARS-CoV-2 in Calu-3
234 cells, we blocked these pathways using 2-DG and 6-diazo-5-oxo-L-norleucine (DON)
235 respectively (Fig 5e) following infection. Infectivity of SARS-CoV-2, quantified as relative *E-*
236 *gene* levels in cells lysates, showed ~50-fold decrease in 2-DG treated cells and >100-fold
237 decrease in DON treated cells (Fig 5f). This was also corroborated with virus production in the
238 cell culture supernatant, quantified by viral *E-gene* levels that decreased by more than 2log10
239 RNA copies/ml in both 2-DG and DON treated cells compared to untreated cells (Fig 5g). While
240 several studies have shown the role of glycolysis on SARS-CoV-2 infection [14, 15], so far there
241 is no direct evidence linking the role of glutaminolysis to replication and spread of SARS-CoV-2
242 and here we show for the first time that both glutaminolysis and glycolysis are essential for
243 SARS-CoV-2 infection.

244 **Role of increased sugars in SARS-CoV-2 infection and the complement system in vitro**

245 To understand the role of sugars like glucose and mannose in SARS-CoV-2 infection, we
246 performed *in vitro* infection assays in Calu-3 cells with varying media concentrations of glucose
247 (11.1, 22.2, 44.4mM) and mannose (0, 11.1, 22.2, 44.4mM) with 0.001moi. We did not observe
248 any statistically significant difference in virus production in the supernatant in the
249 glucose/mannose concentrations tested ($p>0.05$, Fig 6a), while we found a significant reduction
250 in viral *E-gene* expression at cellular level with high glucose concentration of 44.4 mM (Fig 6b,
251 $p<0.05$). Supplementation with high mannose did not cause any significant change in expression
252 of the *E-gene*. Overall, our data indicate that increased glucose levels but not mannose levels has
253 an effect on viral replication *in vitro*.

254 Several studies, including ours, have shown an effect of SARS-CoV-2 infection on complement
255 and coagulation cascades and thrombosis as unique features of COVID-19 infection [7, 19, 20].
256 Temporal transcriptomic and proteomic profiling of SARS-CoV-2 infected Huh7 cells have also
257 revealed an upregulation of proteins involved in complement activation at a later stage of
258 infection [20]. Since complement component C4 is part of the cascade that leads to C3 activation
259 in the classical and MBL pathways, we also studied whether increased glucose/mannose in the
260 media during infection affected upstream events of C3 activation (Fig 6c). This was performed by
261 determining gene expression levels of MBL associated serine protease 2 (*MASP2*) and
262 complement *C4* in Calu-3 cells infected with SARS-CoV-2 (moi 0.001) at different
263 concentrations of glucose and mannose. Mannose availability in the culture medium slightly
264 reduced gene expression of *MASP2* in mock-infected that increased upon infection. However no
265 significant changes in *MASP2* expression were observed compared to the basal condition (Fig
266 6d). An interesting trend was observed with *C4* gene expression (Fig 6e). In mock-infected cells,
267 we observed an increase in *C4* expression with increasing glucose concentrations that decreased
268 dose-dependently following addition of mannose. In the infected cells, a general increase was
269 detected in *C4* expression compared to mock that also followed a similar trend in different
270 glucose and mannose concentrations as was observed in mock-infected cells (Fig 6e). Since
271 COVID-19 patients in this study had high plasma concentrations of glucose and mannose, we
272 also measured *MASP2* and *C4* gene expression in whole blood originating from these patients.
273 No change was observed in *MASP2* expression while a significant decrease in *C4* expression was
274 observed in COVID-19 severe patients compared to HCs (Fig 6f and 6g). Combined, *in vitro* and
275 *in vivo* data indicate a potential role of extracellular glucose and mannose concentrations in
276 complement activation. Further, our data suggest that SARS-CoV-2 infection can

277 transcriptionally repress the C4 system in the presence of high mannose, but this needs further
278 mechanistic investigations.

279

280 **Discussion**

281 In this study, we used metabolomics, proteomics and immunophenotyping to observe the effect
282 of SARS-CoV-2 infection on metabolic dysregulation in COVID-19 patients and performed *in*
283 *vitro* infection in four different cell models to find out potential host metabolic regulation during
284 acute SARS-CoV-2 infection. Our study has shed light on the role of monocytes, especially in
285 severe COVID-19 disease. As expected, COVID-19 patients presented a cytokine storm.
286 Interestingly IL-12 plasma levels were decreased in severe compared to mild COVID-19 patients.
287 Among the carbohydrates, plasma mannose emerged as a biomarker for disease severity, but *in*
288 *vitro* assays showed no effect of mannose on viral replication. Furthermore, host cellular response
289 following SARS-CoV-2 infection identified a strong acute metabolic adaptation in the lung
290 epithelial cells (Calu-3) by modulating central carbon metabolism and indicative of mitochondrial
291 dysfunction that is also observed in severe COVID-19 patients. Glycolysis and glutaminolysis are
292 essential for virus replication and metabolic perturbations of these processes can impede SARS-
293 CoV-2 and could be an attractive antiviral strategy. Finally, SARS-CoV-2 potentially regulates
294 the C4 system transcriptionally in the presence of carbohydrates.

295 As reported, the cytokine storm syndrome is evident in COVID-19 patients [21, 22]. Several
296 plasma pro-inflammatory cytokines including IL-6 were elevated in both mild and severe
297 COVID-19 patients. In our study, though we observed higher levels of soluble IL-12 in mild
298 patients, the severe patients showed IL-12 levels similar to HCs. Elevated plasma levels of IL-12
299 have also been described in hospitalized patients infected with other coronaviruses, such as

300 SARS-CoV and Middle East respiratory syndrome coronavirus (MERS-CoV) [23, 24]. However,
301 to our knowledge, no associations of IL-12 levels with disease severity were reported in these
302 infections. In a recent study on COVID-19 patients on ventilators, the reported low level of IL-12
303 could be caused by impaired monocytes and affect natural killer (NK) cell functions [25, 26]. *In*
304 *vitro* studies on IL-12 administration have shown enhanced host cellular responses that generally
305 promote virus clearance and host recovery from infection [27]. IL-12 also plays a critical role in
306 viral immunity by activating the NK cells and promoting differentiation of Th1 CD4⁺ T-cells.
307 Based on the different levels of IL-12 in COVID-19 patients at varying disease stages, its role in
308 disease severity needs further attention.

309 Both DNA and RNA viruses rewire host cell metabolism by altering central carbon metabolic
310 pathways such as glycolysis, gluconeogenesis, PPP, TCA cycle, amino acid
311 synthesis/degradation, and lipid synthesis. In our metabolomics data, we observed increased
312 glucose, pyruvate and lactate levels in the plasma of COVID-19 patients compared to HCs
313 indicative of toxic metabolic dysregulation during acute phase of infection. Under aerobic,
314 standard growth conditions, primary mammalian cells use glucose for generation of ATP.
315 Glucose is enzymatically broken down to pyruvate that can feed into the TCA cycle in the
316 mitochondria ultimately driving electron transport chain to generate ATP with the help of
317 oxygen.

318 Viral infections including SARS-CoV-2 are known to enhance the glycolytic flux and increase
319 the production of lactate from pyruvate [6, 28, 29]. Viruses can target glycolysis by regulating
320 glucose transporters' expression, which is also vital for immune cell activation during host
321 cellular response [30, 31]. Increased GLUT1 does not only result in higher glucose uptake but
322 also gives rise to increased PPP intermediates that enhance nucleotide pool required for viral
323 replication [5]. GLUT1 transports glucose, mannose, glucosamine and docosahexaenoic acid

324 across the cell membrane [32]. We observed a significant increase in surface expression (MFI) of
325 GLUT1 in CD8⁺ T-cells and intermediate monocytes in COVID-19 severe patients. We also
326 measured surface expression of xCT, a cystine/glutamate antiporter that exchanges glutamate for
327 cystine essential for maintenance of redox balance. While there was a decrease in frequency of
328 only non-classical monocytes expressing xCT in COVID-19 patients, a significant increase in
329 surface expression of xCT in classical and intermediate monocytes COVID-19 patients was
330 noted. To the best of our knowledge, the association of xCT expression in respiratory viral
331 diseases has not been studied before and our data for the first time highlights the crucial role of
332 expression of xCT in monocytes. A growing body of evidence highlights the potential role and
333 metabolic status of monocytes in COVID-19 disease severity [4, 13, 33]. Combining all the data,
334 metabolite transporters, xCT and GLUT1, play an essential role in disease severity that could be
335 linked to higher plasma glucose and mannose levels. The specific changes of metabolic
336 transporters were more prominent in monocytes, indicating that metabolic profile of the different
337 monocytic sub-populations could contribute to mediating the severity of the disease.

338 Plasma mannose emerges as a robust biomarker of disease severity and can also lead to activation
339 of the lectin complement system at a later stage of infection [20]. In addition to mannose, we also
340 observed increased levels of MBL in both COVID-19 patients and convalescent patients
341 compared to the COVID-19 negative individuals. However, no correlation between plasma MBL
342 and mannose were observed in COVID-19 and these two can very well be independent factors.
343 Monomeric mannose is a crucial element of N-linked glycosylation of proteins. Recent studies
344 reported that plasma mannose levels were an indicator of glycogenolysis as well as glucose
345 tolerance and associated with the future risk of developing chronic diseases such as type 2
346 diabetes, cardiovascular diseases, and albuminuria [34, 35]. In our study cohort, the incidence of
347 type 2 diabetes was low in all study groups and can therefore not explain the high plasma

348 mannose levels in COVID-19 patients. This further strongly suggests that increased mannose is
349 an effect of SARS-CoV-2 infection. However, in light of recent research indicating a possibility
350 of a bidirectional link between SARS-CoV-2 and diabetes, it is tempting to speculate that
351 increased mannose has a role to play in new-onset diabetes after SARS-CoV-2 infection [36-39].
352 Mannose can bind to several sugar-binding proteins, called lectins, including C-type lectins, such
353 as MBL, mannose receptor, and DC-SIGN. These receptors recognize carbohydrates, particularly
354 on the surface of microorganisms leading to activation of the complements cascade and
355 phagocytosis [10]. Although N-linked mannose residues have been identified on SARS-CoV-2
356 Spike protein, it is improbable that the elevated plasma mannose levels in the patients would be
357 derived from the virus itself [40]. The processing of endogenous glycoconjugates and their
358 subsequent efflux from the cells are currently thought to be responsible for mannose levels in the
359 blood and steady-state maintenance [41]. Interestingly, a recent study by Heindel et al. describes
360 endogenous high mannose levels as a key mediator of influenza virus-induced pathogenesis and
361 disease severity [42]. High mannose is induced through unfolded protein response pathway and
362 the influenza virus-infected cells are recognized in a high mannose-dependent manner by MBL.
363 Finally, authors state that MBL signaling contributes to disease severity through complement
364 cascade activation and inflammatory response. High mannose and/or high MBL could thus
365 dysregulate the immune system and lead to severe damage associated with disease severity [42].
366 Activation of the complement is one of the features seen in COVID-19, as described in earlier
367 studies [7, 43]. In concordance with that and with Heindel *et al.*, we also noticed increased
368 plasma MBL in COVID-19 and even in healthy convalescent controls compared to HC. This
369 increase in MBL could potentially regulate the complement cascade.

370 In the *in vitro* Calu-3 infection model, most of the proteins from carbohydrate metabolism and
371 PPP were upregulated while most of the proteins of TCA cycle, oxidative phosphorylation, and

372 fatty acid metabolism were downregulated in infected cells compared to the mock-infected
373 controls (Fig 5). Further delineation of the pathways indicated an inefficient mitochondrial
374 metabolism as majority of the TCA cycle enzymes were downregulated in the infected cells. This
375 was in line with the decreased mtDNA copy numbers in severe COVID-19 patients (Fig 5f)
376 indicating a possible mitochondrial dysfunction as reported previously [13, 44-46].
377 The metabolism and concentration of sugars and amino acids such as glucose, mannose,
378 glutamine and glutamate among others, play an important role in cellular metabolic homeostasis
379 and are targeted by viruses for their replication. Recent studies have shown that elevated
380 glycolysis favors SARS-CoV-2 infection and replication [14, 15]. While glutaminolysis has been
381 implicated as a carbon source for other human DNA and RNA viruses [5]. Our data shows for the
382 first time that glutaminolysis is also crucial for SARS-CoV-2 infection and replication. The
383 inhibition of glutaminolysis has a larger effect on viral replication and production compared to
384 the inhibition of the glycolysis in lung cell model (Fig 5f and 5g). Glutaminolysis is a process of
385 converting glutamine to TCA cycle intermediates and also essential for biosynthesis of proteins,
386 lipids and nucleic acids. Some viruses (e.g. Herpes simplex virus 1, human cytomegalovirus,
387 Hepatitis C virus etc) use glutamine as an anaplerotic substrate to replenish TCA cycle via
388 generation of α -ketoglutarate [29, 47]. Recently, researchers have proposed that the metabolic
389 reprogramming of glutamine in SARS-CoV-2 can trigger pathogenesis. They further
390 hypothesized that metabolic intervention of glutaminolysis could be an antiviral strategy for
391 COVID-19 [47-49]. Although the exact underlying mechanism is unknown, our *in vitro* study
392 shows that SARS-CoV-2 replication depends on both glycolysis and glutaminolysis.
393 Finally, to elucidate the effects of extracellular glucose and mannose in both infection of
394 SARS-CoV-2 and its impact on the complement cascade, we established an *in vitro* infection set
395 up with varying media concentrations of glucose and mannose post-infection. Virus production in

396 the cell culture supernatant was unaffected by both glucose and mannose concentrations.
397 However, high extracellular glucose decreased viral infectivity, measured as relative expression
398 of viral *E-gene* in cells. This contradicts the earlier finding that an increase in glucose
399 concentration aids in virus replication [14]. However, it is to be noted, the observations by Codo
400 et al. were made in peripheral monocytes while we performed our experiments in Calu-3 cells.
401 Despite this fact, several studies attempted to isolate infectious virus particles from blood but
402 failed [50, 51] and we were not able to find any residual viral RNA in patients' whole blood cells.
403 Also, blood cell populations do not express the ACE2 or TMPRSS2 (Blood Atlas in the Human
404 Protein Atlas [52]). Thus the infectivity of the blood cell population including lymphocytes and
405 monocytes needs careful consideration [53].

406 In conclusion, our patient based multi-omics studies and *in vitro* analysis emphasizes the need to
407 understand the host metabolic reprogramming due to acute SARS-CoV-2 infection. Among other
408 factors, the role of carbohydrate and amino acid transporters, mainly in the monocytic-
409 macrophage lineages, under the altered central carbon metabolism regulated by
410 AKT/mTOR/HIF-1 signaling may potentially define disease severity. The metabolic alteration in
411 glucose, mannose, lactate, pyruvate, and glutamate in severe COVID-19 cases need further
412 clinical considerations. Changes in these metabolites might have a sustained effect on insulin
413 resistance, type 2 diabetes, neurocognitive impairments, and multiorgan failure which is already
414 reported in COVID-19 infection.

415

416 **Methods**

417 **Experimental Model and Subject Details**

418 **Study designing, patients.** The COVID-19 patients (n=41) who were PCR positive and
419 hospitalized in May 2020, were recruited from the South Hospital, Stockholm. Based on the
420 oxygen requirements the patients were categorized into, 1) Hospitalized-mild (O_2 consumption
421 $<4\text{lit}/\text{min}$) and 2) Hospitalized-severe (O_2 consumption $\geq 4\text{lit}/\text{min}$). The exclusion criteria
422 included known liver cirrhosis, severe renal insufficiency (estimated $eGFR \leq 30\text{mL}/\text{min}/1.73\text{m}^2$),
423 chronic obstructive pulmonary disease, and chronic lung disease leading to habitual $SpO_2 \leq 92\%$.
424 Additionally, COVID-19 PCR negative samples (HC herein, n=31) were also collected. IgG
425 antibody was tested on the HC samples as described previously [51] and ten samples turned out
426 to be SARS-CoV-2 Ab positive further defined as HC-CoV-2 Ab+. The study was approved by
427 regional ethics committees of Stockholm (dnr 2020-01865). All participants gave informed
428 consent. The patient identity was anonymized and delinked before analysis.

429 **Cell lines and viruses.** Human colon adenocarcinoma cell line, Caco-2, and lung
430 adenocarcinoma cell line, Calu-3 (ATCC[®] HTB-55[™]), were purchased from CLS Cell Lines Service
431 GmbH, Germany and LGC Standards, UK, respectively. Hepatocyte-derived carcinoma cell line,
432 Huh7, was obtained from Marburg Virology Lab, Philipps-Universität Marburg, Marburg,
433 Germany matching the STR reference profile of Huh7 [54], and human embryonic kidney cell
434 line, 293FT (Invitrogen). SARS-CoV-2 virus used in this study was the first virus isolated from a
435 Swedish patient[55].

436 **Method Details**

437 **Materials.** All information regarding reagents, antibodies, and critical commercial kits are listed
438 in Table S2.

439 **IgG Antibody detection against SARS-CoV-2.** In brief, 96-well ELISA plates (Nunc
440 MaxiSorp, ThermoFisher Scientific) were coated with SARS-CoV-2 N protein, diluted 1:1000 in

441 50 mM sodium carbonate pH 9.6 (1 ug/ml final concentration), at 4°C overnight. The plates were
442 then blocked for 1h using PBS containing 1% BSA and 2% goat serum (dilution buffer) at 37°C.
443 Serum samples were serially diluted from 1/200 to 1/6400 in dilution buffer and incubated on the
444 plates at 37°C for 1h. Antibodies to the N protein was detected by incubation for 1h at 37°C with
445 anti-human IgG peroxidase (1:30,000, Sigma). The plates were washed three times with PBS
446 with 0,05% Tween-20 between each step. The bound conjugate was visualized using
447 Tetramethylbenzidine (Sigma, USA) substrate. The OD was measured at 450 nm with subtraction
448 of background at 650 nm using a TECAN Infinite M200 plate reader (Tecan, USA).

449 **Plasma inflammation profiling and metabolomics.** The plasma inflammation profiling was
450 performed using proximity extension assay technology targeting 96 inflammation markers by
451 Olink Immuno-Oncology panel (Olink, Sweden). Plasma untargeted metabolomics was
452 performed by Global Metabolomics (HD4) in Metabolon, NC, US as described by us recently
453 [56]. The metabolomics method is ISO 9001:2015 certified and the lab is accredited by the
454 College of American Pathologist (CAP), USA.

455 **Statistical and bioinformatics analysis.** For targeted proteomics data analysis, we used Mann-
456 Whitney U through the R package stats v3.6.1 for pair-wise analysis as the data was not normally
457 distributed. For metabolomics data, dimensionality reduction of all samples were performed with
458 Uniform Manifold Approximation and Projection (UMAP) using R package umap v0.2.6.0 [57].
459 Reduced dimensions of the data were plotted in 2D space using R package ggplot v3.3.2[58]. The
460 metabolite measurements were log2 scaled before differential analysis. Differential analysis was
461 done using R/Bioconductor package limma v3.42.2 [59]. R package MUVR v0.0.973 [60] was
462 used for biomarker discovery. It is a software package that performs predictive multivariate
463 modeling by integrating minimally biased variable selection procedure into repeated double

464 cross-validation architecture. Random forest core modeling was selected from the package for
465 biomarker identification. Minimal-optimal variables selected by the model were considered as
466 biomarkers. Correlation analysis was performed using `corr.test` function from the package `psych`
467 v1.9.12.31 based on Spearman rank correlations. Untargeted protein raw data abundance was first
468 filtered for empty rows and quantile normalized. Differential expression analysis was performed
469 with R package `limma` v3.42.2 [59] to determine proteins with differential abundance.
470 Functional analysis of the proteins was performed using `enrichr` module of python package
471 GSEAPY v 0.9.16 (<https://pypi.org/project/gseapy/>) [61, 62], where all the quantified proteins
472 were considered as background. KEGG 2019 Human gene-set library downloaded from `Enrichr`
473 web resources was used for the enrichment test for molecular pathway analysis. Functional
474 analysis of the metabolites was carried out using Ingenuity Pathway Analysis (IPA) software
475 package. All reported p-values were corrected (*Benjamini-Hochberg*) throughout and considered
476 statistically significant if <0.05 unless otherwise stated.

477 **Data visualization.** Heatmaps were generated using R/Bioconductor package `ComplexHeatmap`
478 v2.2.0 [63]. Violin plots, box plots, bubble plots and volcano plots were made using `geom_violin`,
479 `geom_boxplots`, `geom_point` objects from R package `ggplot2` v3.3.2 respectively. A density plot
480 was created using the function `stat_density_ridges` function from the R package `ggridges` v0.5.2.
481 Alluvial plot was made with `geom_alluvium` function from `ggalluvial` v0.11.3 R package.
482 Correlation pairs plot was made using `ggpairs` function from `GGally` v2.0.0 R package. Network
483 input files were made using R 3.6.3. The network was represented using Cytoscape ver 3.6.1
484 (<https://cytoscape.org/>). Protein-protein interactions were retrieved from STRING Db (v5.0)
485 (<https://string-db.org/>). Only interactions with high confidence (interaction score >0.7) from
486 databases and experiences were kept.

487 **Flow Cytometry.** Peripheral blood mononuclear cells (PBMCs) were subjected to flow
488 cytometry analysis. Samples were thawed in 37°C water bath and washed with flow cytometry
489 buffer (PBS+2% FBS+2mM EDTA). All samples were stained with Live/Dead fixable near IR
490 dye (Invitrogen), and cell surface markers were detected by incubating cells with relevant
491 antibodies for 20min on ice in flow cytometry buffer (antibodies listed in Table S2). All cells
492 were fixed with 2% paraformaldehyde before acquiring a BD FACS Symphony flow cytometer
493 (BD Bioscience). Compensation setup was performed using single-stained controls prepared with
494 antibody-capture beads: Anti-Mouse Ig, κ /Negative Control Compensation Particles Set (BD
495 Biosciences) for mouse antibodies, AbC™ Total Antibody Compensation Bead Kit (Invitrogen)
496 for rabbit antibodies and ArC™ Amine Reactive Compensation Bead Kit (Invitrogen) for use
497 with LIVE/DEAD™ Fixable dead cell stain kits. Flow cytometry data were analyzed and
498 compensated with FlowJo 10.6.2 (TreeStar Inc), Prism 8 (GraphPad Software Inc).

499 **Measurement of mtDNA copy number.** Mitochondrial DNA (mtDNA) copy number was
500 measured using an Absolute Human Telomere Length and Mitochondrial DNA Copy Number
501 Dual Quantification qPCR Assay Kit (ScienCell Research Laboratories, USA). Each 15 μ l qPCR
502 reaction contained 7.5 μ l QuantiNova SYBR green (Qiagen, Sweden), 1 μ l single copy reference
503 (SCR) and mitochondrial primers, 0.1 μ l ROX (passive reference dye), 1.9 μ l DNA/RNA free
504 water and 5 μ l (1ng/ μ l) template DNA. Thermal cycle profile comprised incubation at 50°C for
505 2min and 95°C for 10min before running 40 thermal cycles (95°C for 15s, 54°C for 45 s and
506 72°C for 45s). mtDNA and SCR primers were run on separate plates and each plate contained a
507 serially diluted DNA sample to calculate PCR efficiency. A reference genomic DNA was added
508 on each plate with known mtDNA copy number (925 copies). Each sample was run in duplicates,
509 and relative mtDNA copy number and SCR to reference was calculated by Δ CT (CT target

510 sample - CT reference sample), after adjusting PCR efficiency using the Pfaffl method [64].
511 Finally mtDNA copy number per diploid cell of target sample to reference sample was calculated
512 by $(2^{-\Delta\Delta CT} \times 925)$, where $\Delta\Delta CT$ is $\Delta CT \text{ mtDNA} / \Delta CT \text{ SCR}$.

513 **SARS-CoV-2 infection and proteomics.** In 6-well plate, Calu-3 cells were grown for 72h, and
514 Huh7, 293FT, and Caco-2 cells were grown for 24h in DMEM-high glucose (Sigma-Aldrich,
515 USA) supplemented with 10% FBS (Gibco, USA). The cells were either mock-infected in
516 medium only or infected with SARS-CoV-2 at a multiplicity of infection (moi) of 1 in DMEM-
517 high glucose supplemented with 5% FBS. After 1h the inoculum was removed and was
518 replenished with 2mL of fresh DMEM-high glucose containing 5% FBS. Twenty-four hours
519 post-infection (hpi) the supernatant was removed, and the cells were scrapped in 1mL PBS,
520 centrifuged and the washed cell pellets were lysed in 100 μ L of 2% SDS-lysis buffer (50mM Tris-
521 Cl, 150mM NaCl, 2% SDS and 1mM EDTA) freshly supplemented with protease inhibitor
522 cocktail, phosphatase inhibitor and 1mM DTT. The lysates were heated at 92°C for 10min to
523 deactivate the virus, followed by sonication in a water-bath sonicator for 2min to clear the lysate.
524 Lysates were centrifuged at 13,000rpm for 15min and supernatants were collected. Protein
525 estimation was performed by Bio-rad DC protein assay kit (Bio-Rad Laboratories, USA). The
526 supernatant proteins were used for in-solution digestion and TMT-pro labeled proteomics as
527 described by us previously [7].

528 **Metabolic perturbation and virus infection.** Calu-3 cells were seeded in 24-well plate, and
529 after 72h of seeding, the cells were infected with SARS-CoV-2 at moi of 0.001 for 1h. Following
530 infection, the cells were treated with DMEM (Gibco, USA) which contained pyruvate (1mM) and
531 glutamine (4mM) as the basal carbon source and were supplemented with 5% FBS and different
532 concentrations of glucose (11.1mM, 22.2mM and 44.4mM) (Gibco, USA) and keeping basal

533 glucose concentration at 11.1mM, different concentrations of mannose (11.1mM, 22.2mM and
534 44.4mM) (Sigma-Aldrich, USA). To inhibit glycolysis and glutaminolysis, following 1hpi (moi
535 0.001) the cells were treated with 2-deoxy-D-glucose (2-DG, 10mM) and diazo-5-oxo-L-
536 norleucine (DON, 200µM) respectively. The supernatants were collected after 24hpi and the cells
537 were lysed in TRI reagent (Zymo Research, USA) and stored in -70°C for RNA extraction.

538 **RT-qPCR Analysis.** The virus production and infectivity were determined by qRT-PCR
539 targeting the viral *E-gene* in the supernatant and RNA extracted from the cells. RNA was
540 extracted using Direct-zol™ RNA Miniprep kit according to manufacturer's instructions (Zymo
541 Research, USA). The supernatant or RNA were directly used for one-step RT-qPCR using
542 PrimeDirect™ Probe RT-qPCR Mix (TaKaRa, Japan) according to manufacturer's instructions.
543 Primer and probe sequences for the viral *E-gene* and human *RNaseP* gene are listed in Table S3.
544 To measure gene expression of *MASP2* and *C4* in patient blood, whole blood was collected in
545 Tempus™ Blood RNA Tubes (Applied Biosystems, USA) and RNA was extracted using
546 Tempus™ Spin RNA Isolation Kit (Invitrogen, USA). Quality and concentration of extracted
547 RNA was measured using Nanodrop ND-2000 (Thermo Scientific, USA).

548 The RNA purified from cells and whole blood was reverse transcribed using a High-Capacity
549 cDNA reverse transcription kit (Applied Biosystems, USA) according to manufacturer's
550 instructions. qPCR reactions were performed using KAPA SYBR Fast qPCR kit (KAPA
551 Biosystems, USA) on an Applied Biosystems™ 7500 Fast qPCR machine. Detailed information
552 on primers is included in Table S3.

553 **Plasma MBL Measurement.** MBL levels in patient plasma were determined using Human MBL
554 Quantikine ELISA Kit (R&D Systems) according to manufacturer's instructions. The optical

555 density of each well was determined using NanoQuant Infinite M200 plate reader (Tecan, USA)
556 microplate reader at 450nm with background subtraction at 570nm.

557 **Data and Code Availability.** The scaled normalised metabolomics data can be obtained from the
558 [dx.doi.org/ 10.6084/m9.figshare.13336862](https://dx.doi.org/10.6084/m9.figshare.13336862)

559 Proteomics data can be obtained from the ProteomeXchange Consortium via the PRIDE partner
560 repository with the dataset identifier PXD022847.

561 All the codes are available at github: <https://github.com/neogilab/COVIDOMICS>

562

563

564 **Acknowledgments**

565 The authors would like to thank Elisabet Storgård and Ronnie Ask, Study Nurses, *Södersjukhuset*
566 for their excellent support with patient recruitment and all the clinicians and nurses who are the
567 frontline warriors fighting against COVID-19. Authors acknowledge support from the Proteomics
568 Biomedicum; Karolinska Institute, Solna, for LC-MS/MS analysis.

569

570 **References**

571 1. Thomas T, Stefanoni D, Reisz JA, Nemkov T, Bertolone L, Francis RO, et al. COVID-19
572 infection alters kynurenine and fatty acid metabolism, correlating with IL-6 levels and renal
573 status. *JCI Insight*. 2020;5(14). Epub 2020/06/20. doi: 10.1172/jci.insight.140327. PubMed
574 PMID: 32559180; PubMed Central PMCID: PMC7453907.

- 575 2. Wu D, Shu T, Yang X, Song J-X, Zhang M, Yao C, et al. Plasma metabolomic and
576 lipidomic alterations associated with COVID-19. *National Science Review*. 2020;7(7):1157-68.
577 doi: 10.1093/nsr/nwaa086.
- 578 3. Shen B, Yi X, Sun Y, Bi X, Du J, Zhang C, et al. Proteomic and Metabolomic
579 Characterization of COVID-19 Patient Sera. *Cell*. 2020;182(1):59-72.e15. Epub 2020/06/04. doi:
580 10.1016/j.cell.2020.05.032. PubMed PMID: 32492406; PubMed Central PMCID:
581 PMC7254001.
- 582 4. Su Y, Chen D, Yuan D, Lausted C, Choi J, Dai CL, et al. Multi-omics resolves a sharp
583 disease-state shift between mild and moderate COVID-19. *Cell*. 2020. doi:
584 10.1016/j.cell.2020.10.037.
- 585 5. Mayer KA, Stockl J, Zlabinger GJ, Gualdoni GA. Hijacking the Supplies: Metabolism as a
586 Novel Facet of Virus-Host Interaction. *Front Immunol*. 2019;10:1533. Epub 2019/07/25. doi:
587 10.3389/fimmu.2019.01533. PubMed PMID: 31333664; PubMed Central PMCID:
588 PMC6617997.
- 589 6. Thaker SK, Ch'ng J, Christofk HR. Viral hijacking of cellular metabolism. *BMC Biol*.
590 2019;17(1):59. Epub 2019/07/20. doi: 10.1186/s12915-019-0678-9. PubMed PMID: 31319842;
591 PubMed Central PMCID: PMC6637495.
- 592 7. Appelberg S, Gupta S, Svensson Akusjarvi S, Ambikan AT, Mikaeloff F, Saccon E, et al.
593 Dysregulation in Akt/mTOR/HIF-1 signaling identified by proteo-transcriptomics of SARS-CoV-2
594 infected cells. *Emerg Microbes Infect*. 2020;9(1):1748-60. Epub 2020/07/22. doi:
595 10.1080/22221751.2020.1799723. PubMed PMID: 32691695; PubMed Central PMCID:
596 PMC7473213.

- 597 8. Gordon DE, Jang GM, Bouhaddou M, Xu J, Obernier K, White KM, et al. A SARS-CoV-2
598 protein interaction map reveals targets for drug repurposing. *Nature*. 2020. Epub 2020/05/01.
599 doi: 10.1038/s41586-020-2286-9. PubMed PMID: 32353859.
- 600 9. Barberis E, Timo S, Amede E, Vanella VV, Puricelli C, Cappellano G, et al. Large-Scale
601 Plasma Analysis Revealed New Mechanisms and Molecules Associated with the Host Response
602 to SARS-CoV-2. *Int J Mol Sci*. 2020;21(22). Epub 2020/11/20. doi: 10.3390/ijms21228623.
603 PubMed PMID: 33207699.
- 604 10. Kerrigan AM, Brown GD. C-type lectins and phagocytosis. *Immunobiology*.
605 2009;214(7):562-75. Epub 2009/03/06. doi: 10.1016/j.imbio.2008.11.003. PubMed PMID:
606 19261355; PubMed Central PMCID: PMCPMC2702671.
- 607 11. Monteiro JT, Lepenies B. Myeloid C-Type Lectin Receptors in Viral Recognition and
608 Antiviral Immunity. *Viruses*. 2017;9(3). Epub 2017/03/23. doi: 10.3390/v9030059. PubMed
609 PMID: 28327518; PubMed Central PMCID: PMCPMC5371814.
- 610 12. Weiss HJ, Angiari S. Metabolite Transporters as Regulators of Immunity. *Metabolites*.
611 2020;10(10). Epub 2020/10/23. doi: 10.3390/metabo10100418. PubMed PMID: 33086598;
612 PubMed Central PMCID: PMCPMC7603148.
- 613 13. Gibellini L, De Biasi S, Paolini A, Borella R, Boraldi F, Mattioli M, et al. Altered
614 bioenergetics and mitochondrial dysfunction of monocytes in patients with COVID-19
615 pneumonia. *EMBO Mol Med*. 2020:e13001. Epub 2020/10/21. doi: 10.15252/emmm.202013001.
616 PubMed PMID: 33078545; PubMed Central PMCID: PMCPMC7645870.
- 617 14. Codo AC, Davanzo GG, Monteiro LB, de Souza GF, Muraro SP, Virgilio-da-Silva JV, et
618 al. Elevated Glucose Levels Favor SARS-CoV-2 Infection and Monocyte Response through a
619 HIF-1alpha/Glycolysis-Dependent Axis. *Cell Metab*. 2020;32(3):498-9. Epub 2020/09/03. doi:

- 620 10.1016/j.cmet.2020.07.015. PubMed PMID: 32877692; PubMed Central PMCID:
621 PMCPMC7462530.
- 622 15. Bojkova D, Klann K, Koch B, Widera M, Krause D, Ciesek S, et al. Proteomics of SARS-
623 CoV-2-infected host cells reveals therapy targets. *Nature*. 2020;583(7816):469-72. Epub
624 2020/05/15. doi: 10.1038/s41586-020-2332-7. PubMed PMID: 32408336.
- 625 16. Nunn AVW, Guy GW, Brysch W, Botchway SW, Frasch W, Calabrese EJ, et al. SARS-
626 CoV-2 and mitochondrial health: implications of lifestyle and ageing. *Immunity & Ageing*.
627 2020;17(1):33. doi: 10.1186/s12979-020-00204-x.
- 628 17. Saccon E, Krishnan S, Vinhas BS, Byrareddy SN, Mirazimi A, Neogi U, et al. Replication
629 dynamics and cytotoxicity of SARS-CoV-2 Swedish isolate in commonly used laboratory cell
630 lines. 2020:2020.08.28.271684. doi: 10.1101/2020.08.28.271684 %J bioRxiv.
- 631 18. Fazzini F, Lamina C, Fendt L, Schultheiss UT, Kotsis F, Hicks AA, et al. Mitochondrial
632 DNA copy number is associated with mortality and infections in a large cohort of patients with
633 chronic kidney disease. *Kidney Int*. 2019;96(2):480-8. Epub 2019/06/30. doi:
634 10.1016/j.kint.2019.04.021. PubMed PMID: 31248648.
- 635 19. Eriksson O, Hultstrom M, Persson B, Lipcsey M, Ekdahl KN, Nilsson B, et al. Mannose-
636 Binding Lectin is Associated with Thrombosis and Coagulopathy in Critically Ill COVID-19
637 Patients. *Thromb Haemost*. 2020. Epub 2020/09/02. doi: 10.1055/s-0040-1715835. PubMed
638 PMID: 32871607.
- 639 20. Tiwari R, Mishra AR, Mikaeloff F, Gupta S, Mirazimi A, Byrareddy SN, et al. In silico and
640 In vitro Studies Reveal Complement System Drives Coagulation Cascade in SARS-CoV-2
641 Pathogenesis. *Comput Struct Biotechnol J*. 2020. Epub 2020/11/18. doi:

- 642 10.1016/j.csbj.2020.11.005. PubMed PMID: 33200027; PubMed Central PMCID:
643 PMCPMC7657020.
- 644 21. Gao YM, Xu G, Wang B, Liu BC. Cytokine storm syndrome in coronavirus disease 2019:
645 A narrative review. *J Intern Med*. 2020. Epub 2020/07/23. doi: 10.1111/joim.13144. PubMed
646 PMID: 32696489; PubMed Central PMCID: PMCPMC7404514.
- 647 22. Ragab D, Salah Eldin H, Taeimah M, Khattab R, Salem R. The COVID-19 Cytokine
648 Storm; What We Know So Far. *Front Immunol*. 2020;11:1446. Epub 2020/07/03. doi:
649 10.3389/fimmu.2020.01446. PubMed PMID: 32612617; PubMed Central PMCID:
650 PMCPMC7308649.
- 651 23. Min CK, Cheon S, Ha NY, Sohn KM, Kim Y, Aigerim A, et al. Comparative and kinetic
652 analysis of viral shedding and immunological responses in MERS patients representing a broad
653 spectrum of disease severity. *Sci Rep*. 2016;6:25359. Epub 2016/05/06. doi:
654 10.1038/srep25359. PubMed PMID: 27146253; PubMed Central PMCID: PMCPMC4857172.
- 655 24. Wong CK, Lam CW, Wu AK, Ip WK, Lee NL, Chan IH, et al. Plasma inflammatory
656 cytokines and chemokines in severe acute respiratory syndrome. *Clin Exp Immunol*.
657 2004;136(1):95-103. Epub 2004/03/20. doi: 10.1111/j.1365-2249.2004.02415.x. PubMed PMID:
658 15030519; PubMed Central PMCID: PMCPMC1808997.
- 659 25. Schulte-Schrepping J, Reusch N, Paclik D, Bassler K, Schlickeiser S, Zhang B, et al.
660 Severe COVID-19 Is Marked by a Dysregulated Myeloid Cell Compartment. *Cell*.
661 2020;182(6):1419-40 e23. Epub 2020/08/19. doi: 10.1016/j.cell.2020.08.001. PubMed PMID:
662 32810438; PubMed Central PMCID: PMCPMC7405822.
- 663 26. Osman M, Faridi RM, Sligl W, Shabani-Rad MT, Dharmani-Khan P, Parker A, et al.
664 Impaired natural killer cell counts and cytolytic activity in patients with severe COVID-19. *Blood*

665 Adv. 2020;4(20):5035-9. Epub 2020/10/20. doi: 10.1182/bloodadvances.2020002650. PubMed
666 PMID: 33075136; PubMed Central PMCID: PMCPMC7594380 interests.

667 27. Komastu T, Ireland DD, Reiss CS. IL-12 and viral infections. Cytokine Growth Factor
668 Rev. 1998;9(3-4):277-85. Epub 1999/01/26. doi: 10.1016/s1359-6101(98)00017-3. PubMed
669 PMID: 9918125; PubMed Central PMCID: PMCPMC7129962.

670 28. Shi J, Li Y, Zhou X, Zhang Q, Ye X, Wu Z, et al. Lactate dehydrogenase and
671 susceptibility to deterioration of mild COVID-19 patients: a multicenter nested case-control study.
672 BMC Med. 2020;18(1):168. Epub 2020/06/05. doi: 10.1186/s12916-020-01633-7. PubMed
673 PMID: 32493370; PubMed Central PMCID: PMCPMC7268591.

674 29. Sanchez EL, Lagunoff M. Viral activation of cellular metabolism. Virology. 2015;479-
675 480:609-18. Epub 2015/03/31. doi: 10.1016/j.virol.2015.02.038. PubMed PMID: 25812764;
676 PubMed Central PMCID: PMCPMC4424078.

677 30. Macintyre AN, Gerriets VA, Nichols AG, Michalek RD, Rudolph MC, Deoliveira D, et al.
678 The glucose transporter Glut1 is selectively essential for CD4 T cell activation and effector
679 function. Cell Metab. 2014;20(1):61-72. Epub 2014/06/17. doi: 10.1016/j.cmet.2014.05.004.
680 PubMed PMID: 24930970; PubMed Central PMCID: PMCPMC4079750.

681 31. Palmer CS, Cherry CL, Sada-Ovalle I, Singh A, Crowe SM. Glucose Metabolism in T
682 Cells and Monocytes: New Perspectives in HIV Pathogenesis. EBioMedicine. 2016;6:31-41.
683 Epub 2016/05/24. doi: 10.1016/j.ebiom.2016.02.012. PubMed PMID: 27211546; PubMed
684 Central PMCID: PMCPMC4856752.

685 32. Song W, Li D, Tao L, Luo Q, Chen L. Solute carrier transporters: the metabolic
686 gatekeepers of immune cells. Acta Pharm Sin B. 2020;10(1):61-78. Epub 2020/01/30. doi:

687 10.1016/j.apsb.2019.12.006. PubMed PMID: 31993307; PubMed Central PMCID:
688 PMCPMC6977534.

689 33. Merad M, Martin JC. Pathological inflammation in patients with COVID-19: a key role for
690 monocytes and macrophages. *Nat Rev Immunol.* 2020;20(6):355-62. Epub 2020/05/08. doi:
691 10.1038/s41577-020-0331-4. PubMed PMID: 32376901; PubMed Central PMCID:
692 PMCPMC7201395.

693 34. Mardinoglu A, Stancakova A, Lotta LA, Kuusisto J, Boren J, Bluher M, et al. Plasma
694 Mannose Levels Are Associated with Incident Type 2 Diabetes and Cardiovascular Disease. *Cell*
695 *Metab.* 2017;26(2):281-3. Epub 2017/08/03. doi: 10.1016/j.cmet.2017.07.006. PubMed PMID:
696 28768165.

697 35. Yoshimura K, Hirano S, Takata H, Funakoshi S, Ohmi S, Amano E, et al. Plasma
698 mannose level, a putative indicator of glycogenolysis, and glucose tolerance in Japanese
699 individuals. *J Diabetes Investig.* 2017;8(4):489-95. Epub 2017/02/24. doi: 10.1111/jdi.12622.
700 PubMed PMID: 28084015.

701 36. Chee YJ, Ng SJH, Yeoh E. Diabetic ketoacidosis precipitated by Covid-19 in a patient
702 with newly diagnosed diabetes mellitus. *Diabetes Res Clin Pract.* 2020;164:108166. Epub
703 2020/04/28. doi: 10.1016/j.diabres.2020.108166. PubMed PMID: 32339533; PubMed Central
704 PMCID: PMC7194589 competing financial interests or personal relationships that could
705 have appeared to influence the work reported in this paper.

706 37. Fadini GP, Morieri ML, Boscari F, Fioretto P, Maran A, Busetto L, et al. Newly-diagnosed
707 diabetes and admission hyperglycemia predict COVID-19 severity by aggravating respiratory
708 deterioration. *Diabetes Res Clin Pract.* 2020;168:108374. Epub 2020/08/18. doi:

- 709 10.1016/j.diabres.2020.108374. PubMed PMID: 32805345; PubMed Central PMCID:
710 PMCPMC7428425.
- 711 38. Hollstein T, Schulte DM, Schulz J, Gluck A, Ziegler AG, Bonifacio E, et al. Autoantibody-
712 negative insulin-dependent diabetes mellitus after SARS-CoV-2 infection: a case report. *Nat*
713 *Metab.* 2020;2(10):1021-4. Epub 2020/09/04. doi: 10.1038/s42255-020-00281-8. PubMed PMID:
714 32879473.
- 715 39. Li J, Wang X, Chen J, Zuo X, Zhang H, Deng A. COVID-19 infection may cause ketosis
716 and ketoacidosis. *Diabetes Obes Metab.* 2020. Epub 2020/04/22. doi: 10.1111/dom.14057.
717 PubMed PMID: 32314455; PubMed Central PMCID: PMCPMC7264681.
- 718 40. Shajahan A, Supekar NT, Gleinich AS, Azadi P. Deducing the N- and O- glycosylation
719 profile of the spike protein of novel coronavirus SARS-CoV-2. *Glycobiology.* 2020. doi:
720 10.1093/glycob/cwaa042. PubMed PMID: 32363391; PubMed Central PMCID:
721 PMCPMC7239183.
- 722 41. Sharma V, Freeze HH. Mannose efflux from the cells: a potential source of mannose in
723 blood. *J Biol Chem.* 2011;286(12):10193-200. Epub 2011/01/29. doi: 10.1074/jbc.M110.194241.
724 PubMed PMID: 21273394; PubMed Central PMCID: PMCPMC3060472.
- 725 42. Heindel DW, Koppolu S, Zhang Y, Kasper B, Meche L, Vaiana CA, et al. Glycomic
726 analysis of host response reveals high mannose as a key mediator of influenza severity.
727 *Proceedings of the National Academy of Sciences.* 2020:202008203. doi:
728 10.1073/pnas.2008203117.
- 729 43. Java A, Apicelli AJ, Liszewski MK, Coler-Reilly A, Atkinson JP, Kim AH, et al. The
730 complement system in COVID-19: friend and foe? *JCI insight.* 2020;5(15):e140711. doi:
731 10.1172/jci.insight.140711. PubMed PMID: 32554923.

- 732 44. Thompson E, Cascino K, Ordonez A, Zhou W, Vaghasia A, Hamacher-Brady A, et al.
733 Mitochondrial induced T cell apoptosis and aberrant myeloid metabolic programs define distinct
734 immune cell subsets during acute and recovered SARS-CoV-2 infection. medRxiv. 2020. Epub
735 2020/09/17. doi: 10.1101/2020.09.10.20186064. PubMed PMID: 32935120; PubMed Central
736 PMCID: PMC7491535.
- 737 45. Singh KK, Chaubey G, Chen JY, Suravajhala P. Decoding SARS-CoV-2 hijacking of host
738 mitochondria in COVID-19 pathogenesis. Am J Physiol Cell Physiol. 2020;319(2):C258-C67.
739 Epub 2020/06/09. doi: 10.1152/ajpcell.00224.2020. PubMed PMID: 32510973; PubMed Central
740 PMCID: PMC7381712.
- 741 46. Scozzi D, Cano M, Ma L, Zhou D, Zhu JH, O'Halloran JA, et al. Circulating mitochondrial
742 DNA is an early indicator of severe illness and mortality from COVID-19. JCI Insight. 2021. Epub
743 2021/01/15. doi: 10.1172/jci.insight.143299. PubMed PMID: 33444289.
- 744 47. Hirabara SM, Gorjao R, Levada-Pires AC, Masi LN, Hatanaka E, Cury-Boaventura MF,
745 et al. Host cell glutamine metabolism as a potential antiviral target. Clin Sci (Lond).
746 2021;135(2):305-25. Epub 2021/01/23. doi: 10.1042/CS20201042. PubMed PMID: 33480424.
- 747 48. Mansouri K, Rastegari-Pouyani M, Ghanbri-Movahed M, Safarzadeh M, Kiani S,
748 Ghanbari-Movahed Z. Can a metabolism-targeted therapeutic intervention successfully
749 subjugate SARS-COV-2? A scientific rational. Biomed Pharmacother. 2020;131:110694. Epub
750 2020/09/14. doi: 10.1016/j.biopha.2020.110694. PubMed PMID: 32920511; PubMed Central
751 PMCID: PMC7451059.
- 752 49. Icard P, Lincet H, Wu Z, Coquerel A, Forgez P, Alifano M, et al. The key role of Warburg
753 effect in SARS-CoV-2 replication and associated inflammatory response. Biochimie.

- 754 2021;180:169-77. Epub 2020/11/16. doi: 10.1016/j.biochi.2020.11.010. PubMed PMID:
755 33189832; PubMed Central PMCID: PMC7659517.
- 756 50. Kim JM, Kim HM, Lee EJ, Jo HJ, Yoon Y, Lee NJ, et al. Detection and Isolation of SARS-
757 CoV-2 in Serum, Urine, and Stool Specimens of COVID-19 Patients from the Republic of Korea.
758 Osong Public Health Res Perspect. 2020;11(3):112-7. Epub 2020/06/13. doi:
759 10.24171/j.phrp.2020.11.3.02. PubMed PMID: 32528816; PubMed Central PMCID:
760 PMC7282421.
- 761 51. Varnaité R, García M, Glans H, Maleki KT, Sandberg JT, Tynell J, et al. Expansion of
762 SARS-CoV-2-Specific Antibody-Secreting Cells and Generation of Neutralizing Antibodies in
763 Hospitalized COVID-19 Patients. J Immunol. 2020;205(9):2437-46. Epub 2020/09/04. doi:
764 10.4049/jimmunol.2000717. PubMed PMID: 32878912; PubMed Central PMCID:
765 PMC7576114.
- 766 52. Uhlén M, Fagerberg L, Hallström BM, Lindskog C, Oksvold P, Mardinoglu A, et al.
767 Proteomics. Tissue-based map of the human proteome. Science. 2015;347(6220):1260419.
768 Epub 2015/01/24. doi: 10.1126/science.1260419. PubMed PMID: 25613900.
- 769 53. Borsa M, Mazet JM. Attacking the defence: SARS-CoV-2 can infect immune cells. Nat
770 Rev Immunol. 2020;20(10):592. Epub 2020/08/23. doi: 10.1038/s41577-020-00439-1. PubMed
771 PMID: 32826975; PubMed Central PMCID: PMC7441839.
- 772 54. Rohde C, Becker S, Krahling V. Marburg virus regulates the IRE1/XBP1-dependent
773 unfolded protein response to ensure efficient viral replication. Emerg Microbes Infect.
774 2019;8(1):1300-13. Epub 2019/09/10. doi: 10.1080/22221751.2019.1659552. PubMed PMID:
775 31495285; PubMed Central PMCID: PMC6746283.

- 776 55. Monteil V, Kwon H, Prado P, Hagelkrüys A, Wimmer RA, Stahl M, et al. Inhibition of
777 SARS-CoV-2 infections in engineered human tissues using clinical-grade soluble human ACE2.
778 Cell. 2020.
- 779 56. Babu H, Sperk M, Ambikan AT, Rachel G, Viswanathan VK, Tripathy SP, et al. Plasma
780 Metabolic Signature and Abnormalities in HIV-Infected Individuals on Long-Term Successful
781 Antiretroviral Therapy. *Metabolites*. 2019;9(10). Epub 2019/10/03. doi: 10.3390/metabo9100210.
782 PubMed PMID: 31574898.
- 783 57. Leland M, John, H., Nathaniel, S. & Lukas, G. UMAP: uniform manifold approximation
784 and projection. *Journal of Open Source Software*. 2018;3:861.
- 785 58. Wickham H. *Elegant Graphics for Data Analysis - ggplot2*. New York: New York:
786 Springer-Verlag; 2009.
- 787 59. Ritchie ME, Phipson B, Wu D, Hu Y, Law CW, Shi W, et al. limma powers differential
788 expression analyses for RNA-sequencing and microarray studies. *Nucleic Acids Res*.
789 2015;43(7):e47. Epub 2015/01/22. doi: 10.1093/nar/gkv007. PubMed PMID: 25605792; PubMed
790 Central PMCID: PMC4402510.
- 791 60. Shi L, Westerhuis JA, Rosen J, Landberg R, Brunius C. Variable selection and validation
792 in multivariate modelling. *Bioinformatics*. 2019;35(6):972-80. Epub 2018/08/31. doi:
793 10.1093/bioinformatics/bty710. PubMed PMID: 30165467; PubMed Central PMCID:
794 PMC419897.
- 795 61. Kuleshov MV, Jones MR, Rouillard AD, Fernandez NF, Duan Q, Wang Z, et al. Enrichr: a
796 comprehensive gene set enrichment analysis web server 2016 update. *Nucleic Acids Res*.
797 2016;44(W1):W90-7. Epub 2016/05/05. doi: 10.1093/nar/gkw377. PubMed PMID: 27141961;
798 PubMed Central PMCID: PMC4987924.

799 62. Subramanian A, Tamayo P, Mootha VK, Mukherjee S, Ebert BL, Gillette MA, et al. Gene
800 set enrichment analysis: a knowledge-based approach for interpreting genome-wide expression
801 profiles. *Proc Natl Acad Sci U S A*. 2005;102(43):15545-50. Epub 2005/10/04. doi:
802 10.1073/pnas.0506580102. PubMed PMID: 16199517; PubMed Central PMCID:
803 PMCPMC1239896.

804 63. Gu Z, Eils R, Schlesner M. Complex heatmaps reveal patterns and correlations in
805 multidimensional genomic data. *Bioinformatics*. 2016;32(18):2847-9. Epub 2016/05/22. doi:
806 10.1093/bioinformatics/btw313. PubMed PMID: 27207943.

807 64. Pfaffl MW. A new mathematical model for relative quantification in real-time RT-PCR.
808 *Nucleic Acids Res*. 2001;29(9):e45. Epub 2001/05/09. doi: 10.1093/nar/29.9.e45. PubMed
809 PMID: 11328886; PubMed Central PMCID: PMCPMC55695.

810

811 **Figure Legends**

812 **Fig 1. Targeted plasma proteomics in COVID-19 patients.** (a) Heatmap of Z-score
813 transformed quantitative measurements of all proteins detected by the immuno-oncology panel.
814 Column annotation represents each patient sample and their corresponding groups and pairs of
815 statistical analysis. Rows are proteins hierarchically clustered based on the Euclidean distance
816 and complete linkage method. Names of proteins which are identified as significant in any of the
817 statistical analysis printed. (b) KEGG pathway enrichment analysis results of significantly
818 changed proteins between healthy control (HC + HC-CoV-2 Ab+) and COVID-19 (hospitalized
819 mild+hospitalized severe) groups. (c) Violin plot of significantly regulated (Mann-Whitney U
820 test) proteins between hospitalized mild and hospitalized severe, *adj p<0.05, **adj p<0.01.

821 **Fig 2. Untargeted global plasma metabolomics in COVID-19 patients** (a) Sample distribution
822 for quantitative metabolite measurements plotted in 2-dimensional space after performing
823 dimensionality reduction using UMAP. (b) Stacked bar plots visualizing percentage of
824 metabolites significantly changed between healthy control (HC + HC-CoV-2 Ab+) and COVID-
825 19 (hospitalized mild + hospitalized severe) group concerning their corresponding super-
826 pathways and sub-pathways. (c) Metabolic set enrichment analysis using the significantly
827 enriched metabolites between HCs and COVID-19 patients. The size of the bubble indicates
828 adjusted p-values. (d) Heatmap of log₂ scaled and Z-score transformed measurements of
829 metabolites significantly changed between healthy control (HC + HC-CoV-2 Ab+) and COVID-
830 19 (hospitalized mild + hospitalized severe) groups. Column annotation represents each patient
831 sample and the corresponding groups. Row annotation represents super pathways of the
832 metabolites. Rows are metabolites hierarchically clustered based on Euclidean distance and
833 complete linkage method.

834 **Fig 3. Untargeted plasma metabolites differing between the mild and severe hospitalized**
835 **COVID19 patients. (a)** Heatmap of log₂ scaled, and Z-score transformed significantly changed
836 metabolites between hospitalized mild and hospitalized severe groups. Column annotation
837 represents each patient sample and the corresponding groups. Rows are metabolites hierarchically
838 clustered based on Euclidean distance and complete linkage method. **(b)** Alluvial plot
839 representing pathways resulted from IPA pathway enrichment analysis using all metabolites that
840 differs significantly between hospitalized mild and severe groups. **(c)** Volcano plot showing all
841 the metabolites that differ significantly between hospitalized mild and hospitalized severe groups.
842 **(d)** Box plots of key metabolites glutamate, glucose and mannose **(e)** Schematic representation of
843 the key steps of glycolysis, mannose and glutamate metabolism and TCA cycle. **(f)** Box plots of
844 soluble mannose-binding lectin levels in patients' plasma. P-values determined by Mann-
845 Whitney U test.

846 **Fig 4. Glucose, mannose and glutamate transporters in COVID-19 severity: (a)** Percentage
847 of total lymphocytes and monocytes in all 4 patient groups; **(b)** Percentage of PBMC
848 subpopulations, CD3⁺ T-cells of lymphocytes, CD4⁺ T-cells (of CD3⁺ cells) CD8⁺ T-cells (of
849 CD3⁺ cells), classical monocytes (CM, CD14⁺CD16⁻ of monocytes), intermediate monocytes
850 (IM, CD14⁺CD16⁺ of monocytes) and non-classical monocytes (NCM, CD14⁻CD16⁺ of
851 monocytes). Median values are indicated by lines. **(c)** Density plot of percentage of CD8⁺ T-cells,
852 IM and NCM expressing GLUT1. Histograms show percentage of cells expressing GLUT1
853 (x-axis) and GLUT1 read density of each sample (y-axis). The median percentage of cells
854 expressing GLUT1 is shown for each patient group. **(d)** MFI of GLUT1 in CD8⁺ T-cells, IM and
855 NCM in all four patient groups. **(e)** Density plot of percentage of CM, IM and NCM expressing
856 xCT. Histograms show percentage of cells expressing xCT (x-axis) and xCT read density of each

857 sample (y-axis). The median percentage of cells expressing xCT is shown for each patient group.
858 **(f)** MFI of xCT in CM, IM and NCM in all four patient groups. In all the panels the median
859 values are indicated by lines, p-values are determined by Mann-Whitney U test, *p<0.05,
860 **p<0.01, and ***p<0.001.

861 **Fig 5. Cell-specific regulation of central carbon metabolic pathways by SARS-CoV-2: (a)**
862 Bubble plots of protein set enrichment analysis (adj. p<0.05) restricted to metabolic pathways
863 showing highly upregulated (red) and downregulated (green) proteins in SARS-CoV-2 infected
864 Calu-3 cells compared to mock-infected cells. Bubble size is relative to number of proteins. **(b)**
865 Network analysis of proteins from glycolysis/gluconeogenesis, fructose and mannose metabolism
866 and TCA cycle that were significantly different in SARS-CoV-2 infected and mock-infected
867 Calu-3 cells. Rectangular shapes represent the three pathways. Circular shapes show each protein
868 that is either upregulated (red) or downregulated (green) in infected cells compared to mock-
869 infected cells. The size of the circle indicates fold-change. Lines denote connection of each
870 protein to its respective pathway and connection between each protein-protein (STRING,
871 confidence>0.7). **(c)** Schematic map of the glycolysis/gluconeogenesis, fructose and mannose
872 metabolism and TCA cycle. Red indicates significantly upregulated proteins and green indicates
873 significantly downregulated proteins in SARS-CoV-2 infected Calu-3 cells. **(d)** mtDNA copy
874 number in whole blood cells in all 4 patient groups. Median values are indicated by lines, p-
875 values are determined by Mann-Whitney U test, *p<0.05. **(e)** Schematic of inhibitors of
876 metabolic pathways, 2-DG inhibits glycolysis and DON inhibits glutaminolysis. **(f, g)** Viral load
877 of SARS-CoV-2 determined by RT-qPCR targeting the viral *E-gene* is measured in **(f)** cells
878 lysates and **(g)** cell culture supernatants, at moi 0.001 in Calu-3 cells treated with 2-DG or DON

879 as indicated. The data is represented as mean±SEM of two individual experiments, triplicates in
880 each experiment. P-values are determined by student T-test, *p<0.05, ***p<0.001.

881 **Fig 6. Role of glucose and mannose in SARS-CoV-2 infectivity and complement pathways:**

882 Viral load of SARS-CoV-2 determined by RT-qPCR targeting the viral *E-gene* is measured in (a)
883 cell culture supernatants, and (b) cell lysates at moi 0.001 infection of Calu-3 cells grown in
884 different glucose and mannose concentrations (mM) as indicated. The data is represented as
885 mean±SEM of two independent experiments, duplicates in each experiment. P-values are
886 determined by student T-test, *p<0.05. (c) Schematic of complement cascade showing pathway
887 upstream of C3 and C5 activation. Gene expressions of (d) *MASP2*, and (e) *C4* in SARS-CoV-2
888 infected (moi 0.001) and mock-infected Calu-3 cells at different glucose and mannose
889 concentrations (mM) as indicated. All gene expression data in Calu-3 cells (viral *E-gene*, *MASP2*
890 and *C4*) at each glucose/mannose concentration were compared with baseline expression at
891 11.1mM glucose, 0mM mannose and data represented as mean±SEM. Gene expressions of (f)
892 *MASP2*, and (g) *C4* in whole blood of HC, HC-CoV-2 Ab+, COVID-19 hospitalized mild and
893 hospitalized severe patients determined by RT-qPCR. Median values are indicated by line, p-
894 values are determined by Mann-Whitney-U test, *p<0.05 and **p<0.01.

895 **Supplementary Files:**

896 **Table S1.** Clinical Features of the study population

897 **Table S2:** List of reagents, kits and antibodies

898 **Table S3:** List of primer and probe sequences

899 **Fig S1:** The IgG Ab showed 10 of the HC were CoV-2 Ab-positive.

900 **Fig S2:** Metabolite profile of amino acids altered in COVID-19 patients. Line within box plots
901 represents median values, *p<0.05, **p<0.01, ***p<0.001.

902 **Fig S3:** Levels of metabolites related to glycolysis/gluconeogenesis and fructose and mannose
903 metabolism and the TCA cycle

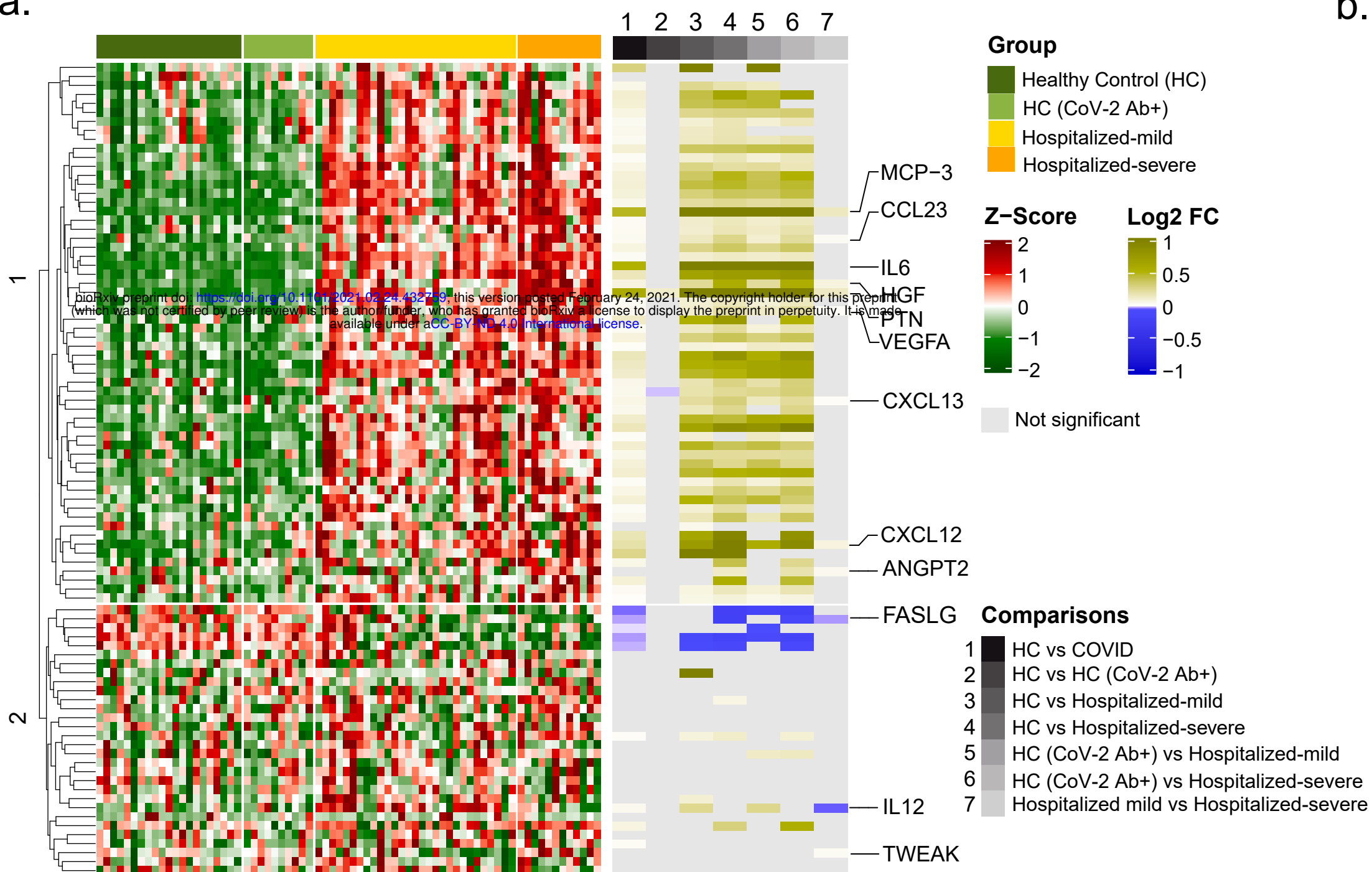
904 **Fig S4:** Biomarker of the COVID-19 severity identified by MVUR. The size of the bubble
905 indicates rank. Box plot of the biomarkers indicating the level in HCs and COVID-19 patients.:
906 update

907 **Fig S5:** Differential protein abundance in Calu-3 cells following SARS-CoV-2 infection after
908 24h. The analysis was restricted to glycolysis/gluconeogenesis, fructose and mannose metabolism
909 and the TCA cycle.

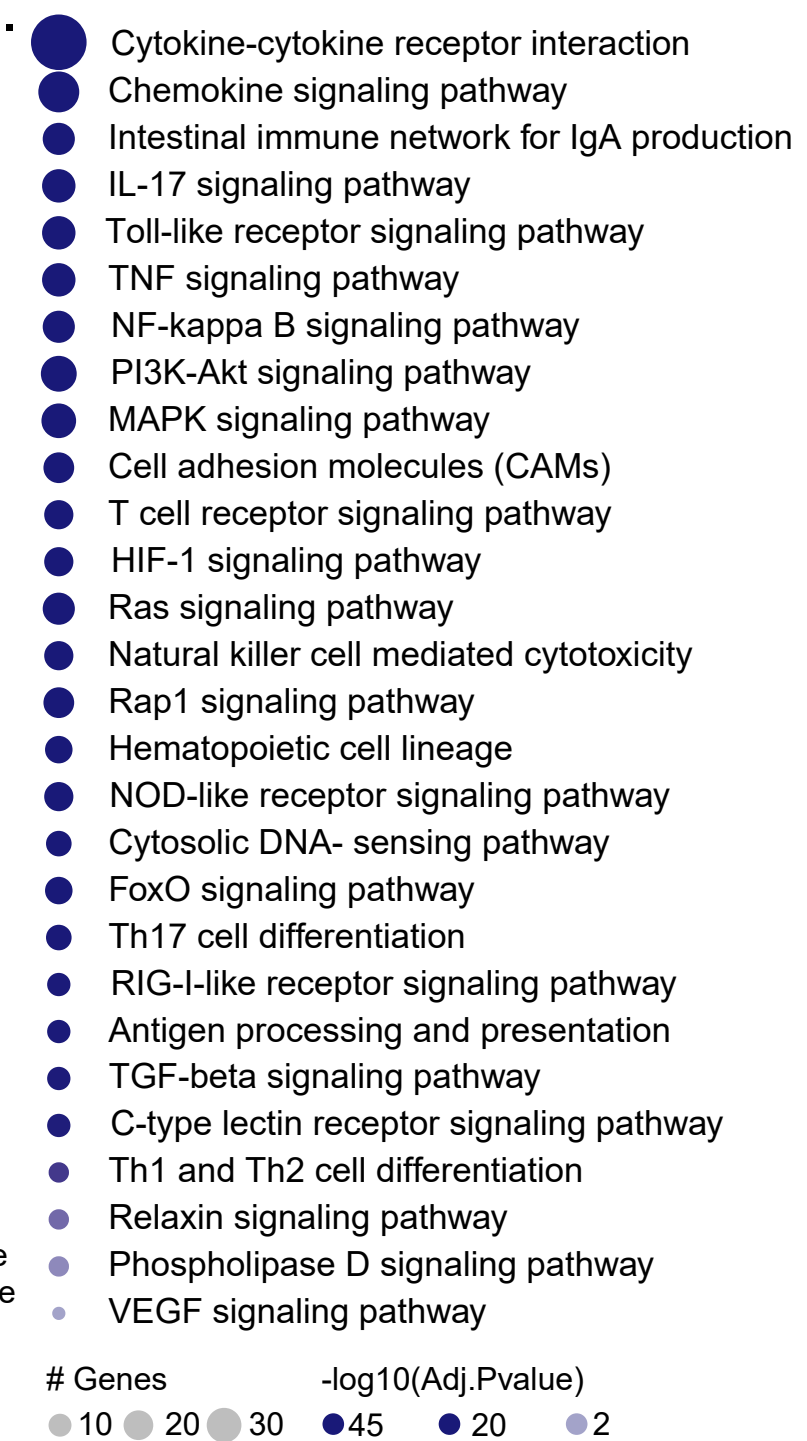
910 **Fig S6:** Differential protein abundance in Caco-2, Huh7 and 293FT cells following SARS-CoV-
911 2 infection after 24h. The analysis was restricted to glycolysis/gluconeogenesis, fructose and
912 mannose metabolism and the TCA cycle.

913 **Fig S7:** Gating strategy of flow cytometry data.

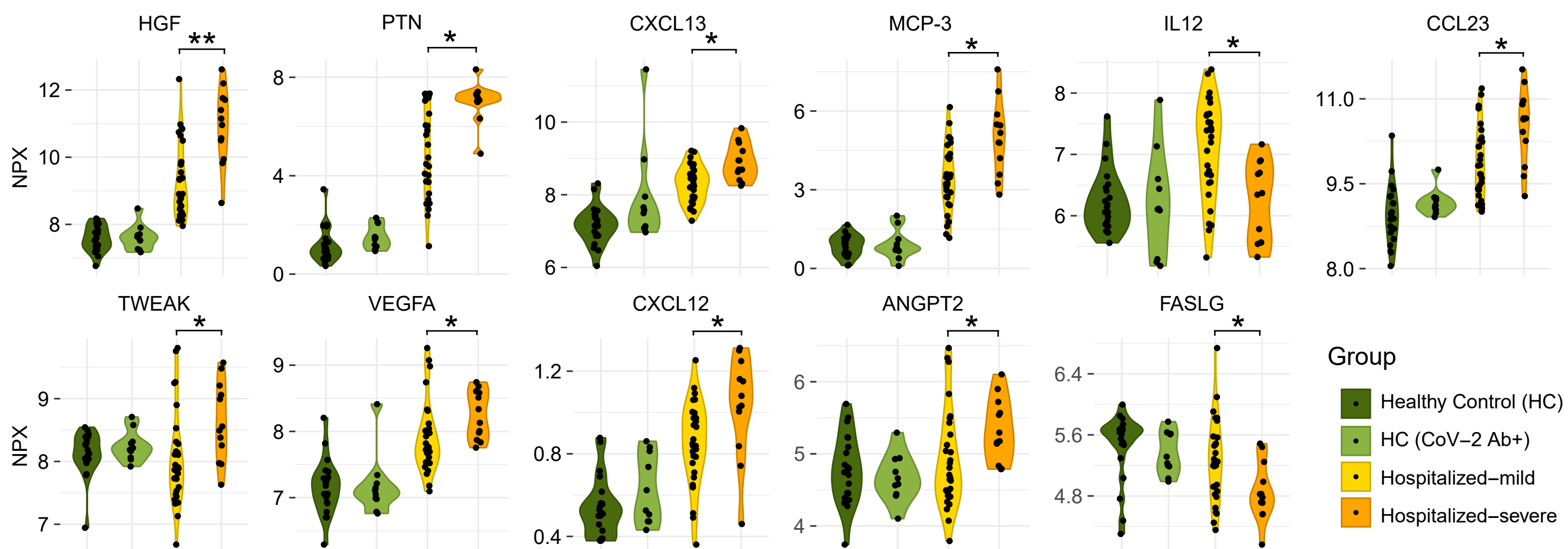
a.

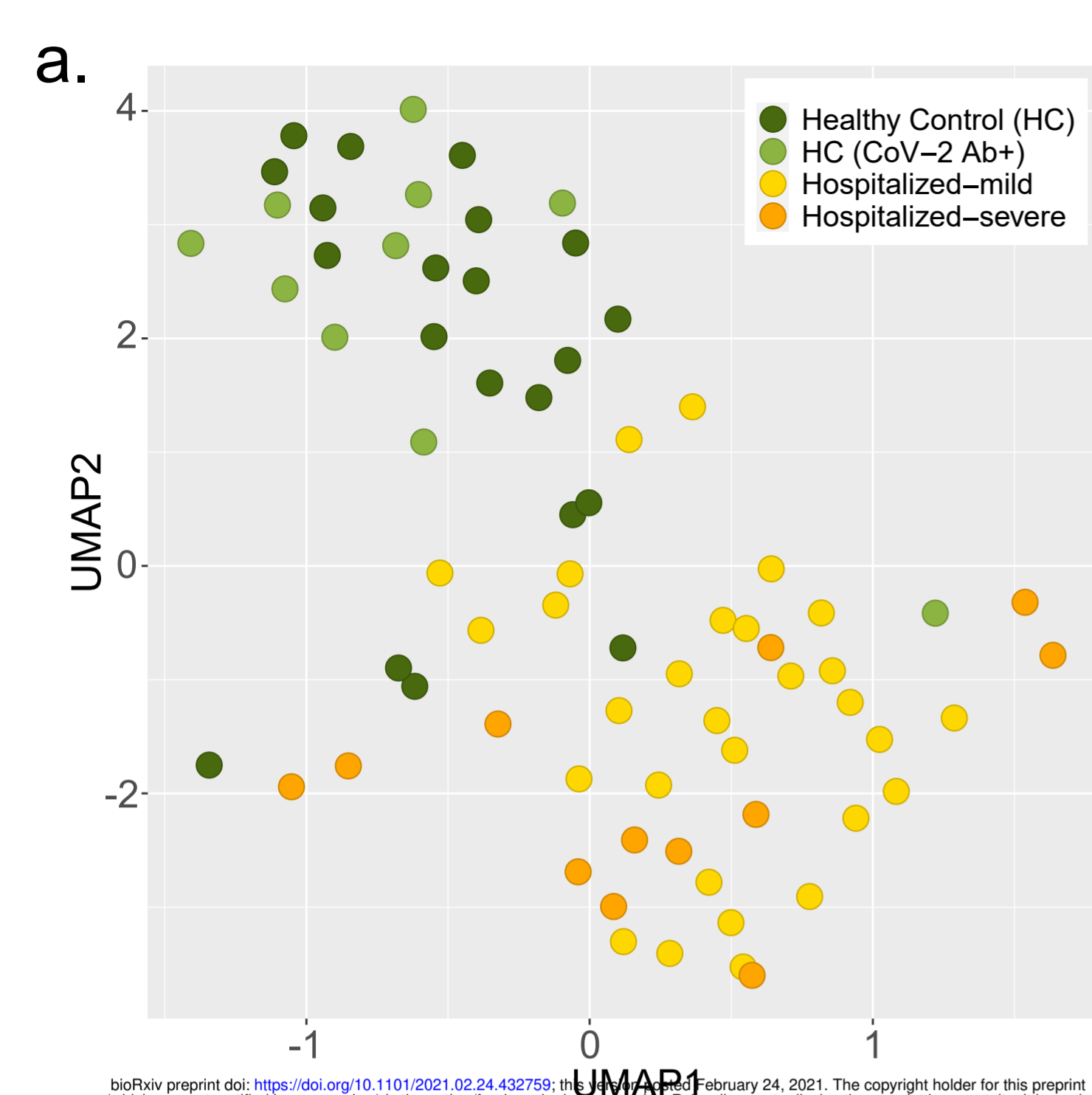


b.

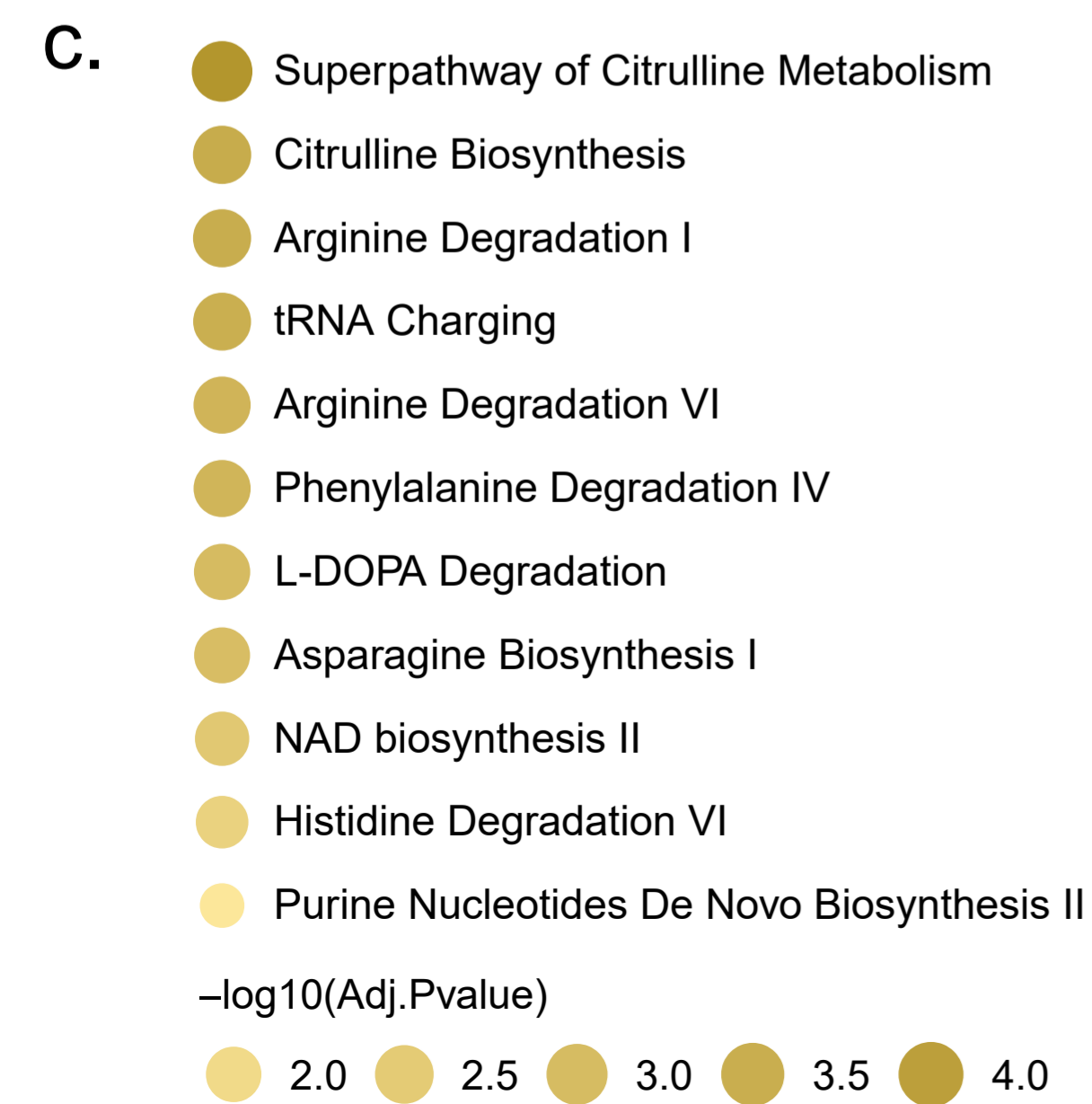
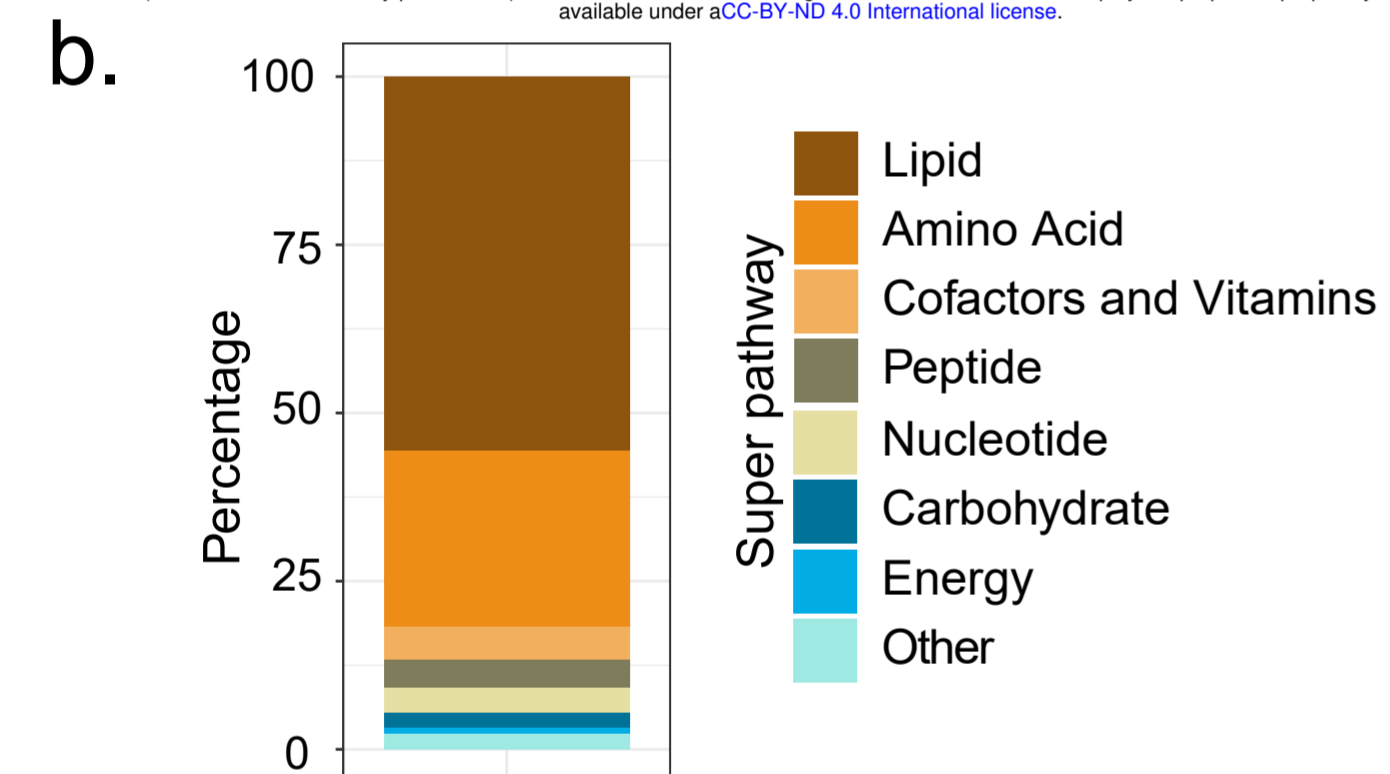


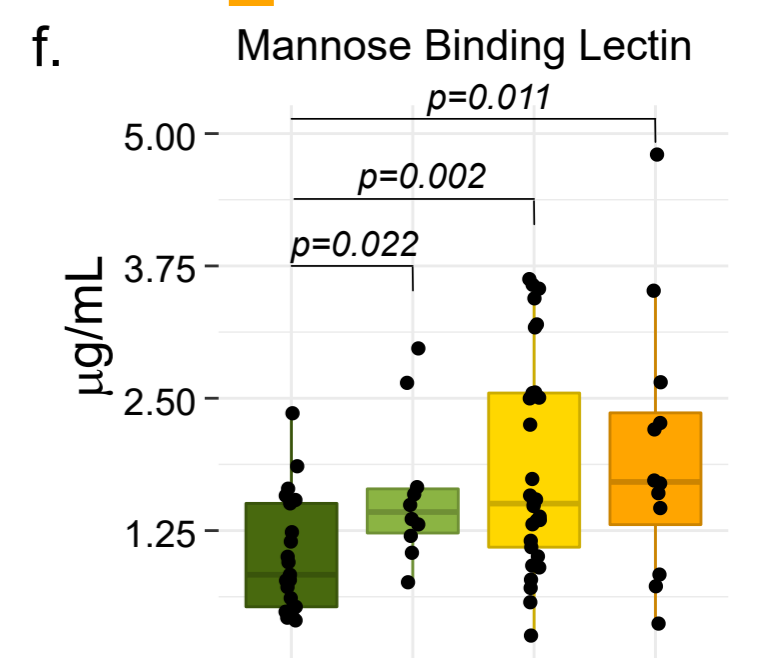
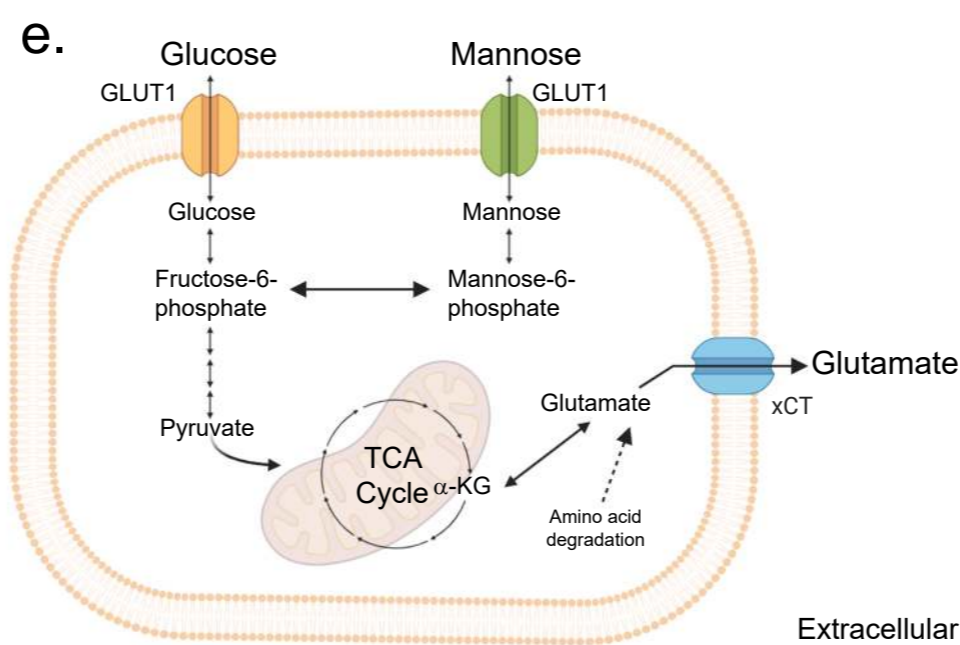
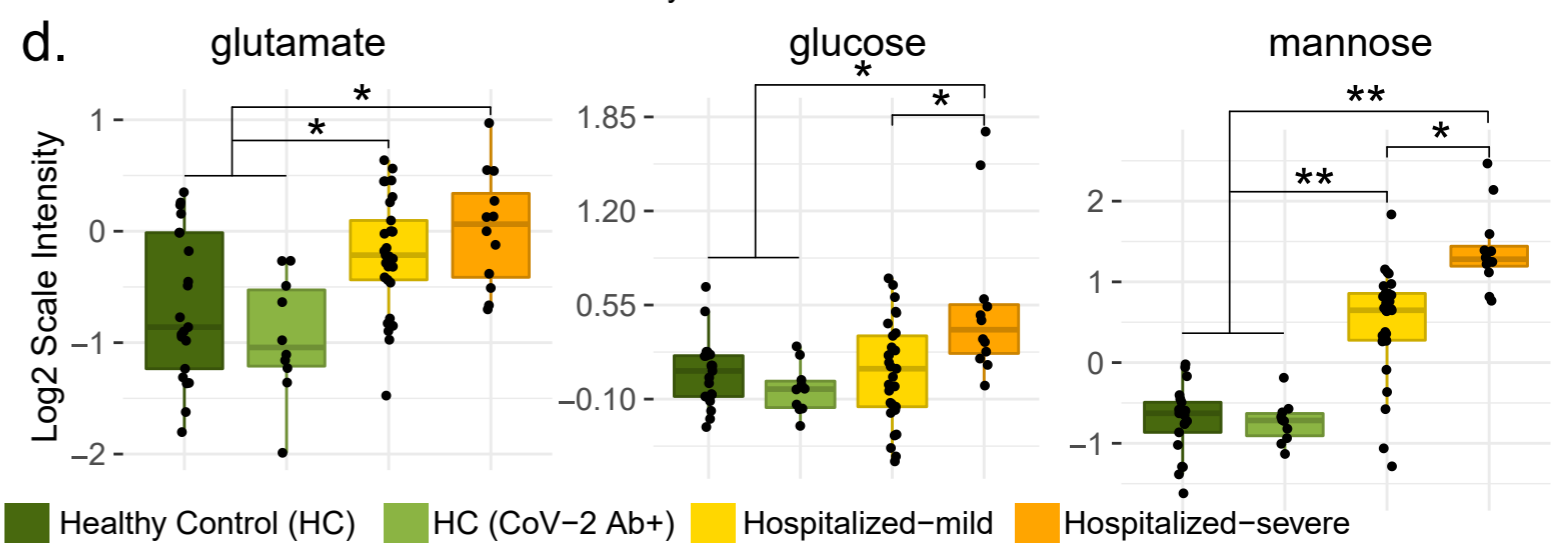
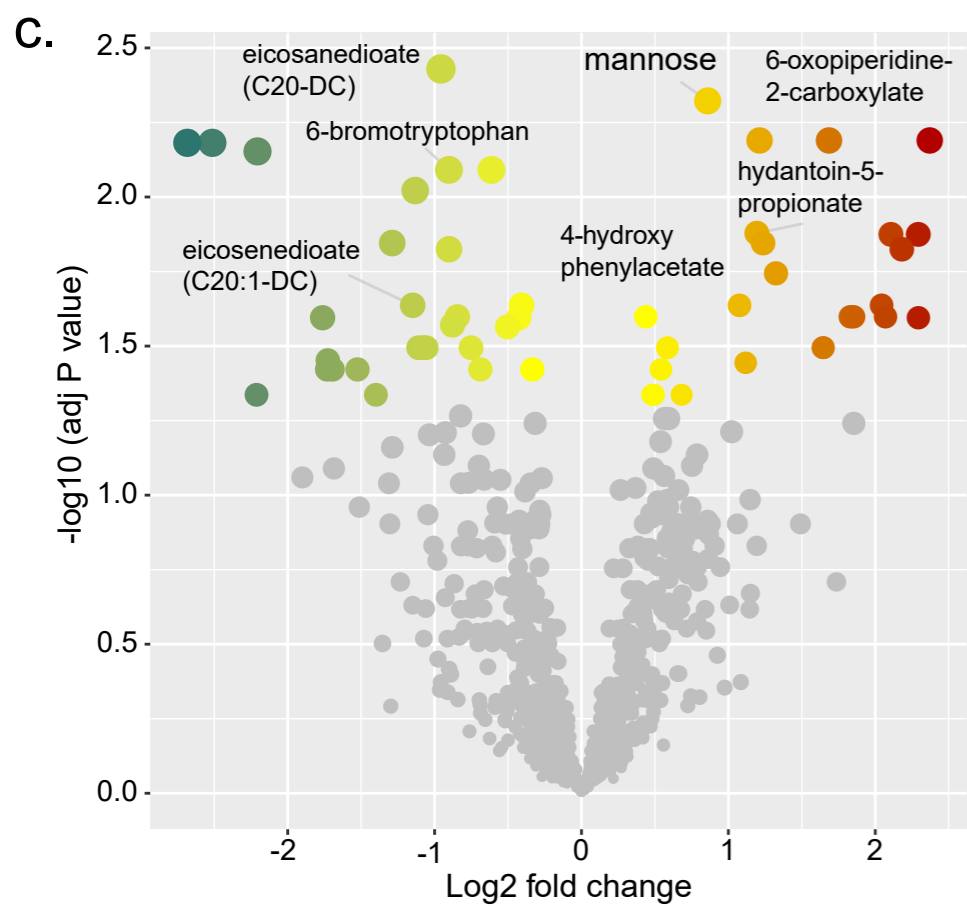
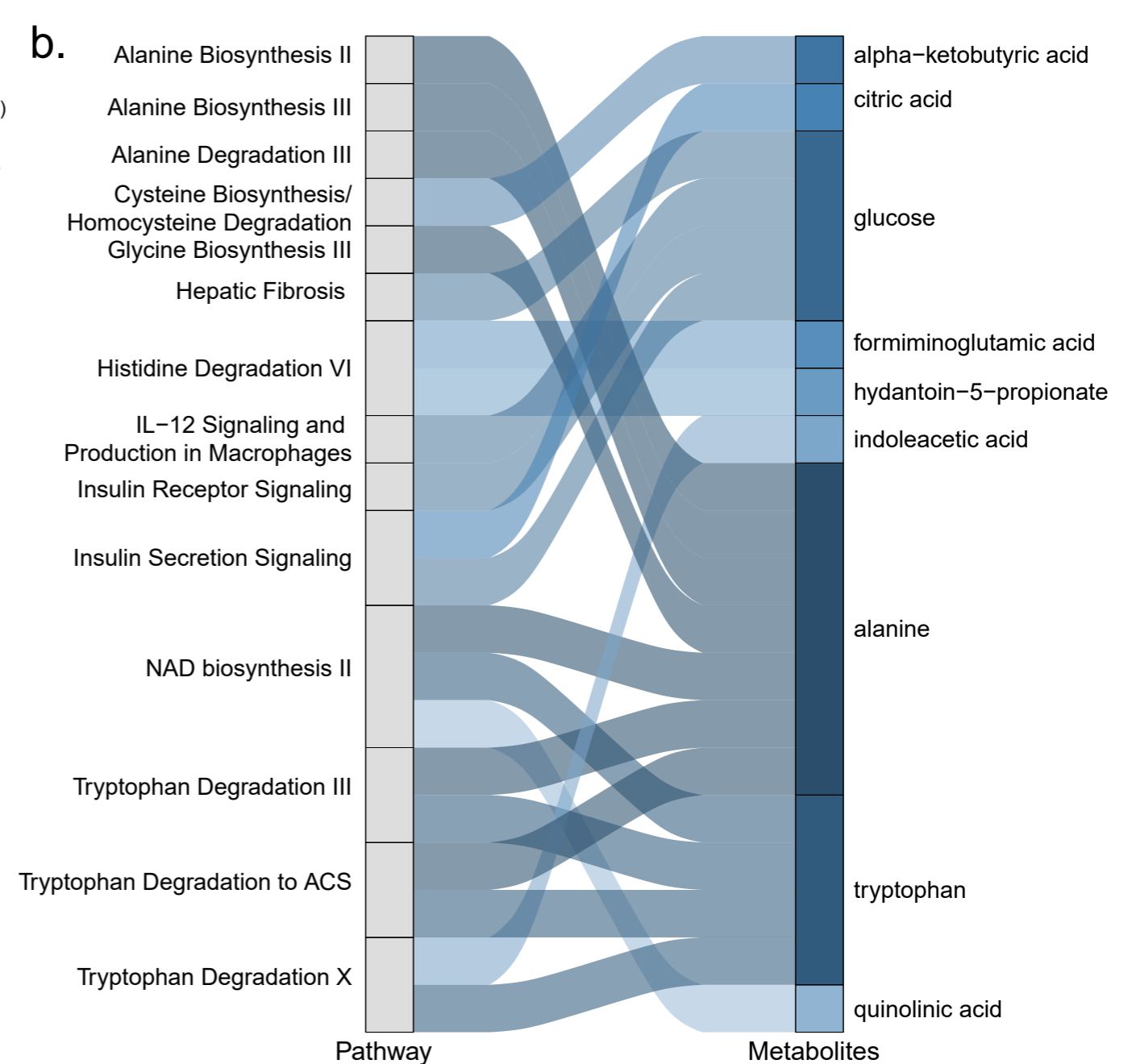
c.

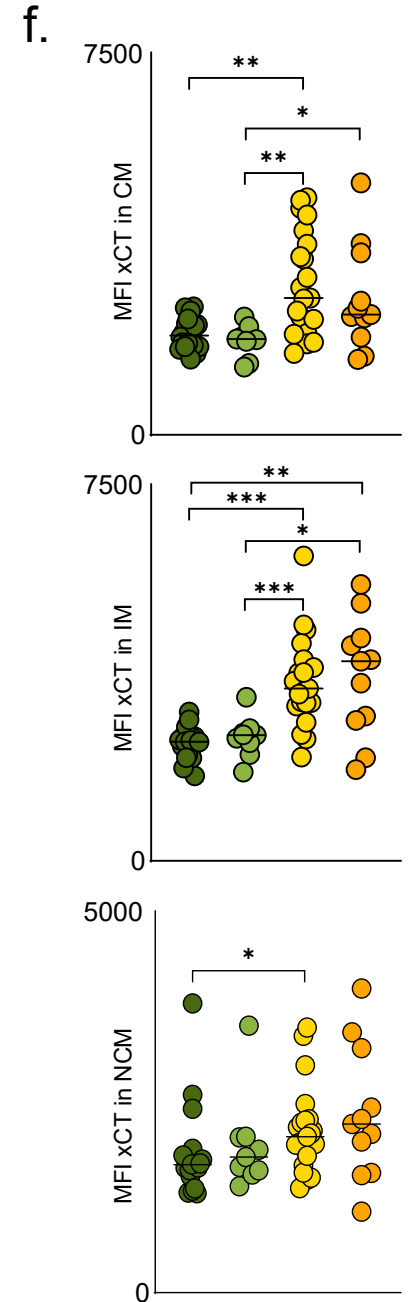
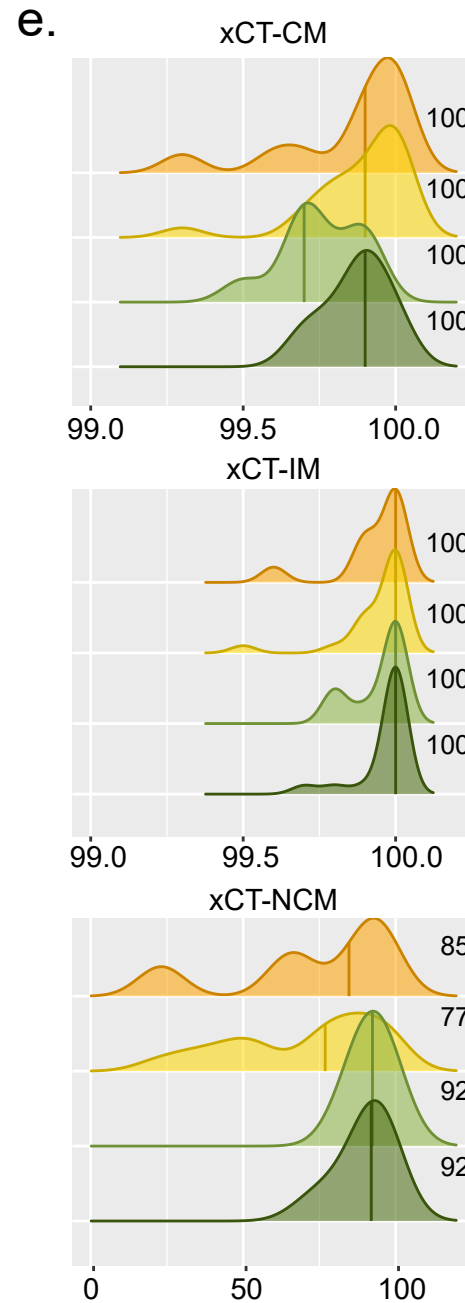
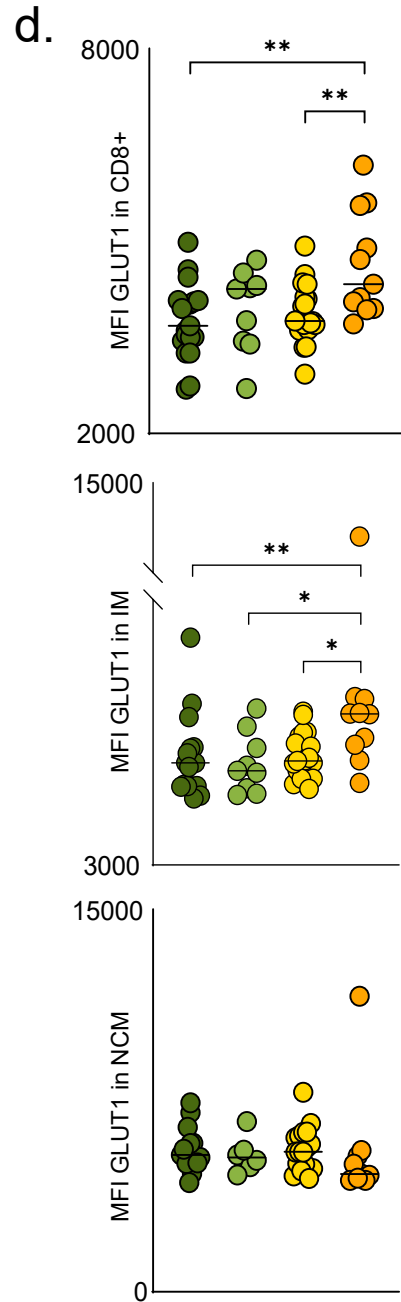
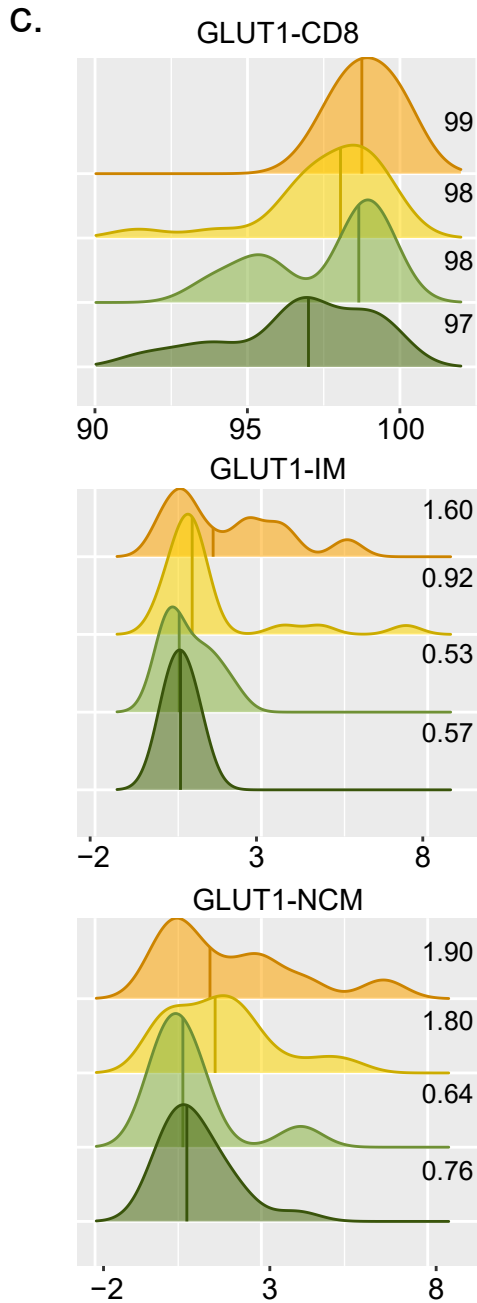
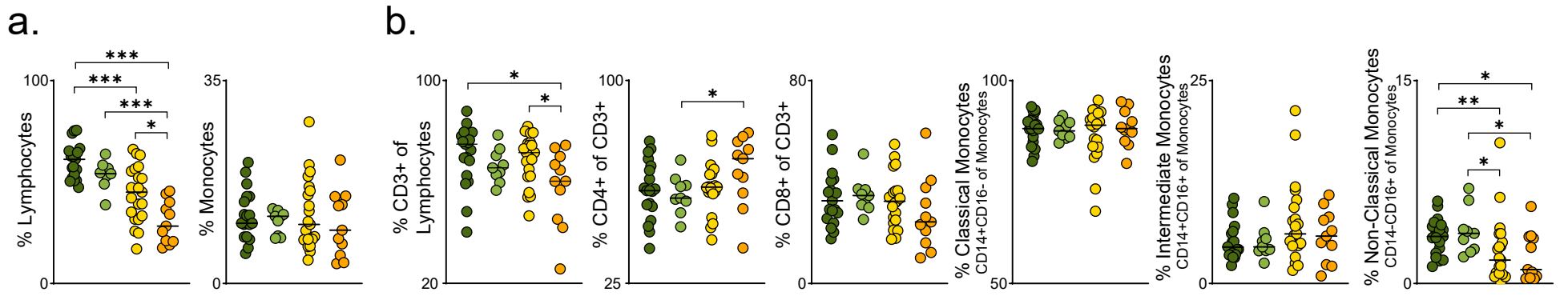




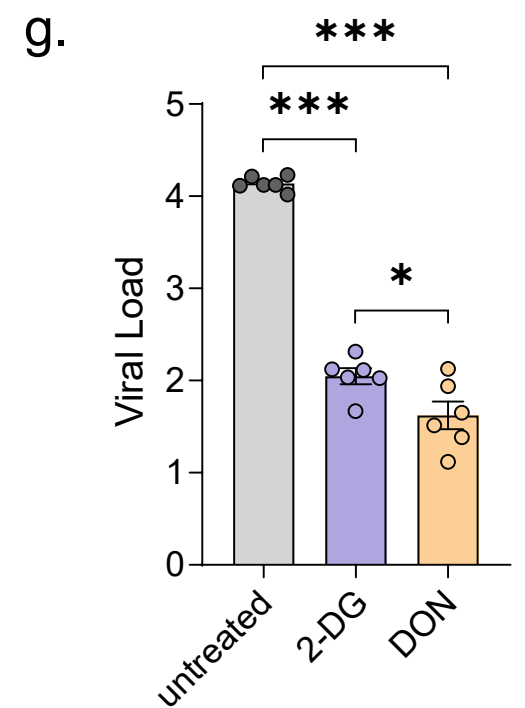
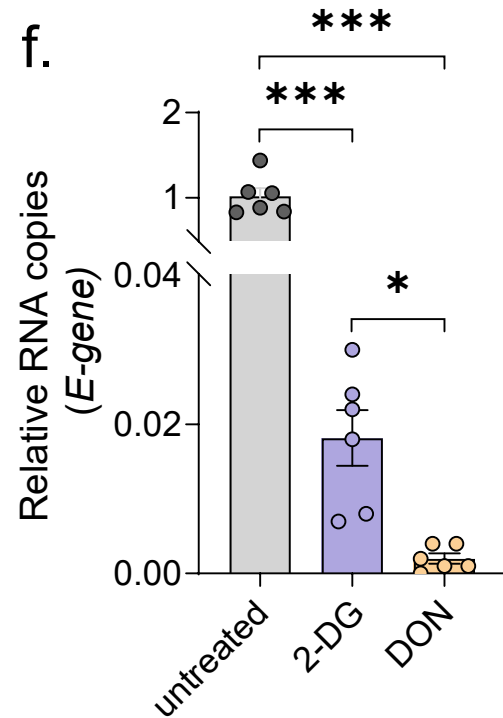
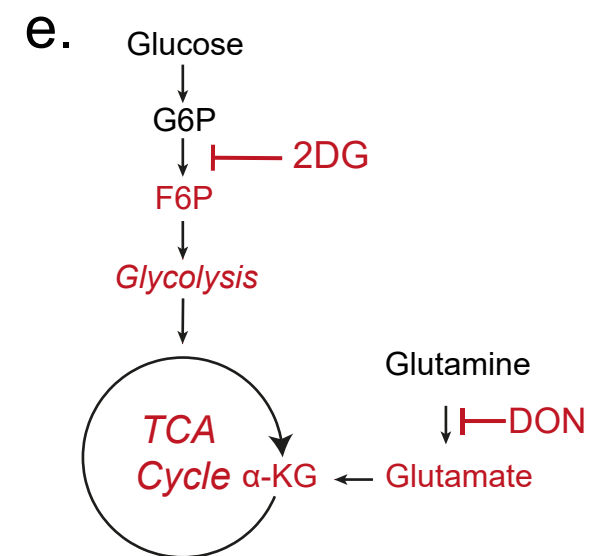
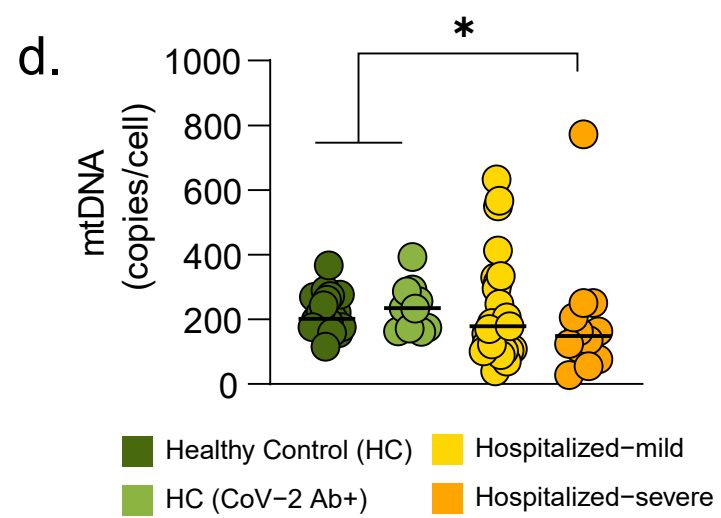
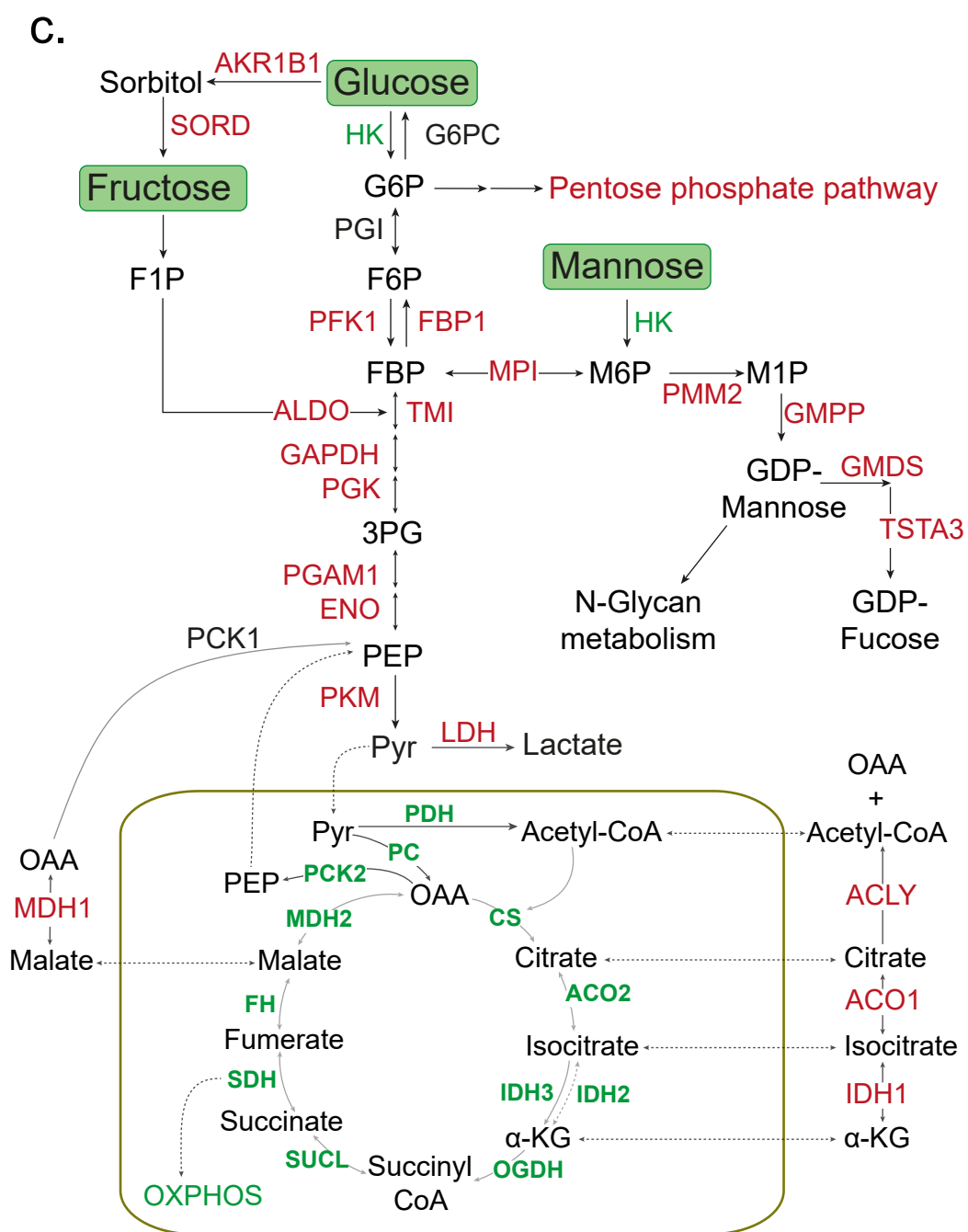
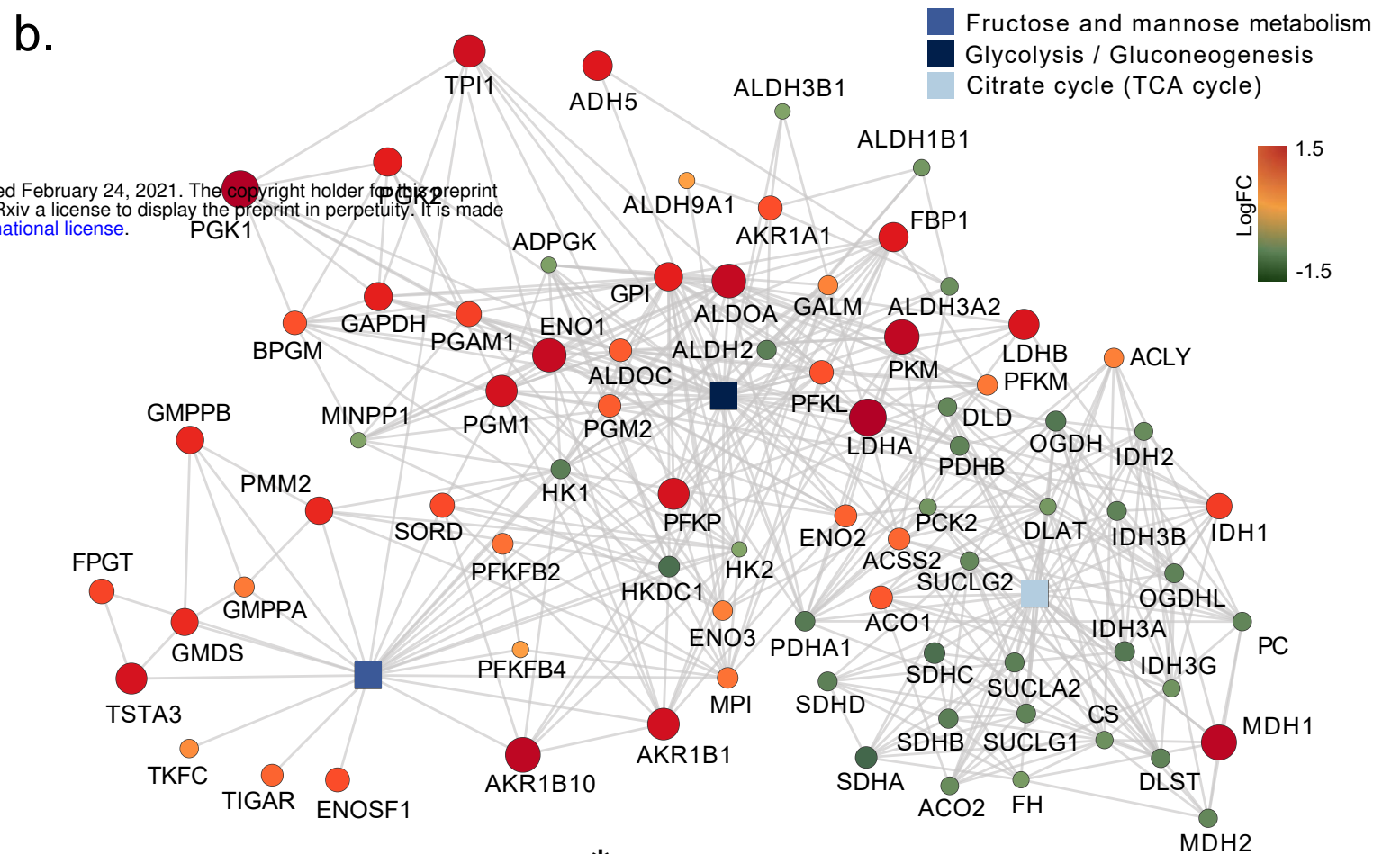
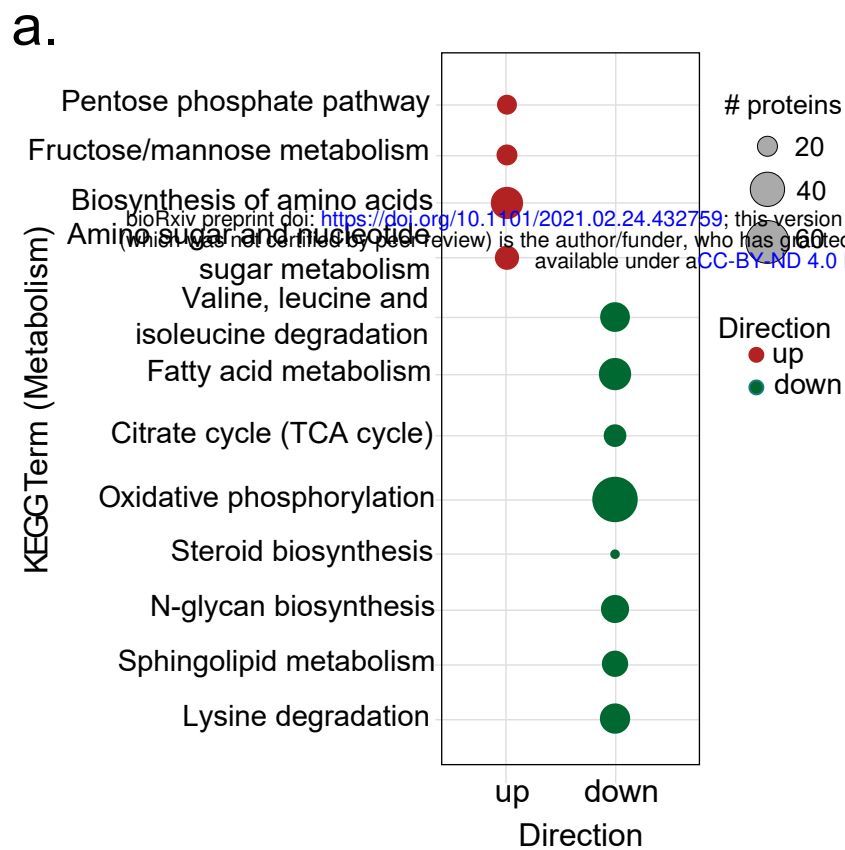
bioRxiv preprint doi: <https://doi.org/10.1101/2021.02.24.432759>; this version posted February 24, 2021. The copyright holder for this preprint (which was not certified by peer review) is the author/funder, who has granted bioRxiv a license to display the preprint in perpetuity. It is made available under aCC-BY-ND 4.0 International license.

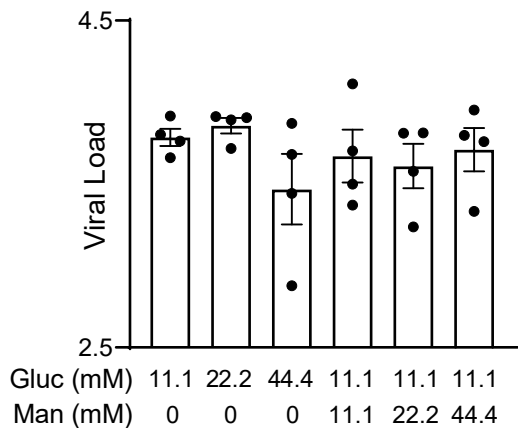
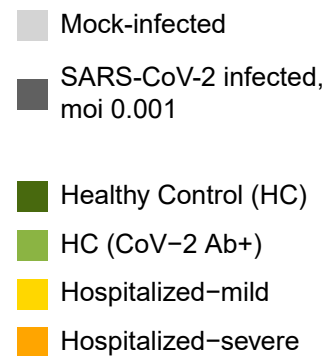
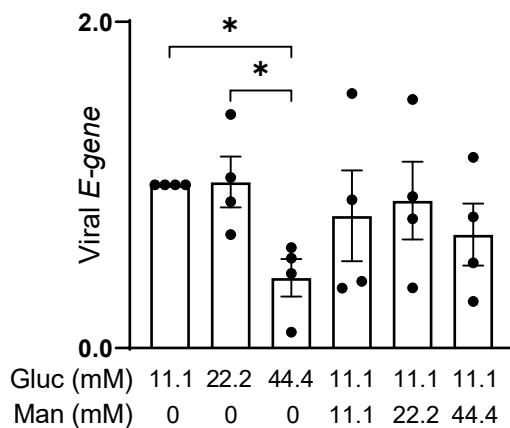
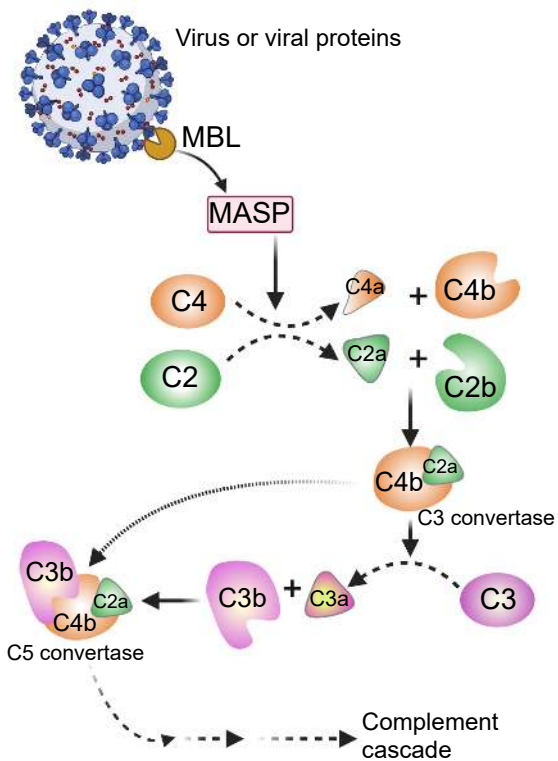
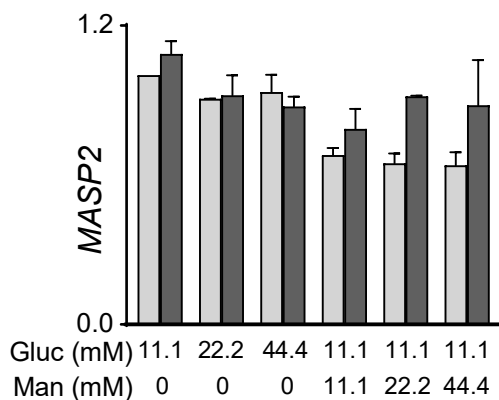
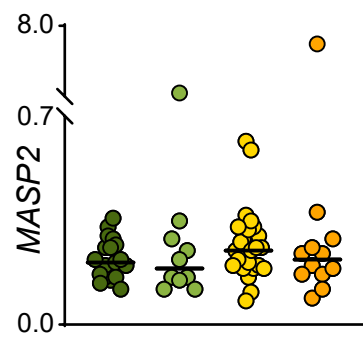
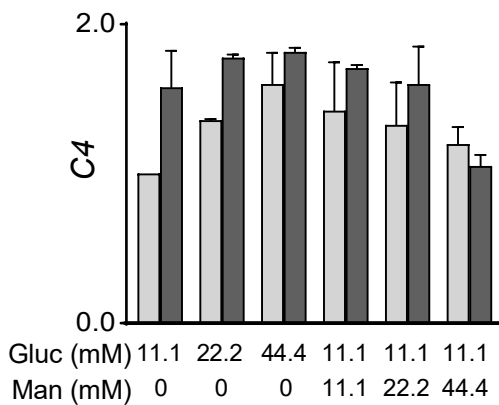






■ Healthy Control (HC)
 ■ HC (CoV-2 Ab+)
 ■ Hospitalized-mild
 ■ Hospitalized-severe



a.**b.****c.****d.****f.****e.****g.**